The magnitude of adaptive type-2 immunity is locally constrained via a Gata3^{high} Treg – ILC2 axis

Julie Stockis[1]†, Thomas Yip,[1]†, Julia Moreno-Vicente[1]†, Oliver Burton[2,3], Youhani Samarakoon[1], Martijn J. Schuijs[1], Shwetha Raghunathan[1], Celine Garcia[1], Weike Luo[1], Sarah K. Whiteside[3], Shaun Png[1], Charlotte Simpson[1], Stela Monk[1], Ashley Sawle[1], Kelvin Yin[1], Johanna Barbieri[1], Panagiotis Papadopoulos[1], Hannah Wong[4], Hans-Reimer Rodewald[5], Timothy Vyse[6], Andrew N.J. McKenzie[7], Mark S. Cragg[8], Matthew Hoare[1,9], David R. Withers[10], Hans Jörg Fehling[11], Rahul Roychoudhuri[3], Adrian Liston[2,3] and Timotheus Y.F. Halim[1,]*.

[1] University of Cambridge, CRUK Cambridge Institute; Cambridge, CB2 0RE, UK.

[2] Immunology Programme, The Babraham Institute; Cambridge, CB22 3AT, UK.

[3] Department of Pathology, University of Cambridge; Cambridge, CB2 1QP, UK.

[4] Department of Veterinary Medicine, University of Cambridge; Cambridge, CB3 0ES, UK.

[5] Division of Cellular Immunology, German Cancer Research Center; Heidelberg, Germany.

[6] Department of Medical and Molecular Genetics, King's College London; London SE1 9RT, UK.

[7] Medical Research Council, Laboratory of Molecular Biology; Cambridge, CB2 0QH, UK.

[8] Antibody and Vaccine Group, Centre for Cancer Immunology, School of Cancer Sciences, Faculty of Medicine, University of Southampton; Southampton, SO16 6YD, UK.

[9] University of Cambridge, Department of Medicine; Cambridge CB2 0QQ, UK.

[10] University of Birmingham, Institute of Immunology and Immunotherapy; Birmingham B15 2TT, UK.

[11] Institute of Immunology, University Hospital Ulm; Ulm, Germany.

† equal contributions.

Corresponding author:
* Tim.Halim@cruk.cam.ac.uk

Abstract

Regulatory T cells (Tregs) control adaptive immunity and restrain type-2 inflammation in allergic disease; nevertheless, little is known about how Tregs locally coordinate their function in the inflamed niche. Here we show that group 2 innate lymphoid cells (ILC2) are critical orchestrators of Treg function. Using spatial, cellular, and molecular profiling of the type-2 inflamed niche we found that ILC2 and Tregs engage in multifaceted cellular dialogue that directly enforces the local accumulation of Gata3^{high} Tregs, which are transcriptionally and functionally adapted to the type-2 environment. Genetic interruption of ILC2-Treg communication resulted in uncontrolled type-2 inflammation after allergen exposure. Mechanistically, we attributed this to the ability of Gata3^{high} Tregs to modulate the local bioavailability of the co-stimulatory molecule OX40L, which controlled effector memory Th2 cell numbers. Hence, ILC2-Treg interactions serve as a critical feedback mechanism to control adaptive type-2 immunity.

One Sentence Summary

Treg-mediated constraint of adaptive type-2 inflammation is contingent on local dialogue with ILC2.

Introduction

Unlike epithelial or mesenchymal cells, whose cellular densities are constrained by the structural boundaries of tissues and their microenvironment, immune cell densities are largely dictated by local inflammatory mediator or mitogen abundances (*1*). As such, inflamed organs can rapidly and profoundly increase immune cell numbers; while this capacity evolved to counter pathogens, concomitant regulatory mechanism are equally important to maintain a fine balance between protective and destructive inflammation. Regulatory T cells (Tregs) are centrally involved in this homeostatic process, although many questions persist about how diverse Treg subsets locally curtail different types of inflammation (*2*).

Treg deficiencies or depletion often result in unrestrained type-2 inflammation (*3–5*), although it remains unclear if specific Treg subsets are elicited to suppress CD4^{+} T helper type-2 (Th2) cells. Shared transcription factors between Tregs and Th2 cells, such as *Irf4* (*6*) and *Gata3* (*7*) are important for Treg function in models of type-2 inflammation; however, Treg-specific deletions of these transcription factors are confounded by their graded or low constitutive expression, and concomitant homeostatic or developmental roles (*8*). Nevertheless, it is likely that shared transcriptional programmes promote co-localisation of effector Th2 cells and Tregs in the type-2 inflamed niche, although this paradigm is better defined for type-1 or type-17 inflammation (*9–11*). Relatedly, regulatory-to-effector T cell ratios strongly influence local control of allergic inflammation (*12*); moreover, while allergenic peptides underpin pathogenic Th2 cell-driven inflammation, less is known about the mechanisms that guide Treg-mediated restraint of adaptive type-2 immunity (*13*, *14*).

2

Epithelial or stromal cell sensing of tissue stress initiates type-2 immune activation via the release of the alarmin interleukin (IL)-33, which acts on both innate and adaptive type-2 immune cells expressing its receptor ST2. While IL-33 strongly promotes type-2 immunity, it also mediates the suppressive functions of ST2+ regulatory Tregs (15, 16), and organ-homeostatic roles of ST2+ tissue-resident Tregs (17–19). While IL-33 can directly influence ST2+ Treg function, other reports suggest that indirect effects of IL-33 guide the overall Treg response (20–22). Specifically, expression of the co-stimulatory ligand OX40L (*Tnfsf4*) by ILC2 is critical for simultaneous Th2 and Treg expansion in type-2 inflammation (20). It remains uncertain if OX40 expression by Tregs is required for their local expansion, and, more importantly, why ILC2 can simultaneously engage Th2 cell-driven effector and regulatory immunity.

Using spatial, cellular, and molecular profiling of the type-2 inflamed niche, we found that both Th2 and Gata3high Tregs closely associated with ILC2. Notably, Gata3high Tregs were greatly enriched in type-2 inflammation due to a multifaceted ILC2-Treg dialogue involving CCL1-CCR8 and OX40L-OX40 signalling. Unbiased profiling of OX40L expressing cells using a gene-reporter identified ILC2 as the major cellular source in both the type-2 inflamed lung and its draining lymph node. Using OX40 Treg-conditional knockout mice, we found that Gata3high Treg expansion was greatly impaired in response to IL-33-driven allergic inflammation, and moreover, resulted in the profound local expansion of type-2 immune cells. Mechanistically, we found that Gata3high Tregs can directly modulate OX40L surface expression on ILC2; the increased bioavailability of this co-stimulatory molecule in OX40 Treg-deficient mice underpinned unrestrained expansion of effector memory Th2 cells in the lung and associated lymph-nodes. Thus, ILC2 serve as a critical local orchestrator of Treg-mediated constraint of adaptive type-2 immunity.

Results

The inflamed type-2 immune niche is typified by Gata3high innate and adaptive lymphocytes that possess both effector and regulatory functions.

Both innate and adaptive type-2 effector lymphocytes depend on the transcription factor Gata3 for their development and function. Gata3 can also be expressed by Tregs, and Gata3high Tregs are greatly amplified alongside Gata3high Th2 and ILC2 in the lungs after exposure to IL-33 or allergens such as papain, house dust mite, or ragweed pollen extract (Fig. 1A, S1A, S1B). Focussing on Gata3high Tregs, we observed that this subset was largely CD62L-CD44+ and highly expressed KLRG1, a marker associated with tissue-resident Tregs (Fig. 1A, S1C). By intravenous administration of anti-CD45.2 mAb we confirmed that Gata3high KLRG1+ Tregs showed increased tissue-residency compared to

Gata3^{low} KLRG1$^-$ Tregs, while lung ILC2 were almost exclusively tissue-resident (Fig. S1D). Next, using multiplex IF microscopy of lung sections we identified CD3$^+$Foxp3$^+$ Tregs, CD3$^+$Gata3$^+$Foxp3$^-$ Th2 cells, and CD3$^-$Gata3$^+$ ILC2 after IL-33 administration (Fig. S1E). Co-staining for CD31 and Collagen 1 confirmed that ILC2 localised close to the adventitial sheath surrounding large vessels and airways (*23*), where we also observed Tregs and Th2 cells (Fig. 1B). Image analysis indicated that Treg and Th2 cells localised closer to ILC2 than CD3$^+$Gata3$^-$Foxp3$^-$ conventional T (Tconv) cells (Fig. 1C). Similarly, 2-photon microscopy of *Il5^{tdTom}Foxp3^{YFP}* mouse lung explants showed that ILC2 and Tregs co-localised after IL-33 administration (Fig. 1D, S1F). Hence, we hypothesized that both effector and regulatory Gata3^{high} lymphocytes enact transcriptional programmes that enforce their co-localization, and potential dialogue, in the type-2 inflamed niche.

To isolate innate and adaptive type-2 lymphocytes we used *Gata3^{YFP}* reporters (which retain endogenous *Gata3* expression (*24*)) and generated *Gata3^{YFP}Foxp3^{RFP}* mice (Fig. 1E). We could accurately identify distinct Gata3^{high} CD4$^+$ T cell-types and ILC2, which all expanded in the lung after intranasal IL-33 administration; using flow-sorting we purified these and Gata3^{low} Treg and CD4$^+$ Tconv cell subsets for bulk RNA-seq analysis (Fig. S1G-J).

Transcriptomically, we found that ILC2, Tregs, Th2 and Tconv cells expressed their respective lineage-associated genes (Fig. 1F). Reassuringly, *Gata3* expression levels matched that of the reporter; moreover, Th2 cells and Gata3^{high} Tregs expressed high transcript levels of *Tnfrsf4* (OX40), *Klrg1* and *Cd44*, while *Sell* (CD62L) was amplified in Gata3^{low} Tregs and Tconv cells, matching our flow-cytometry data (Fig. S1C). Interestingly, Th2 as well as Gata3^{high} and Gata3^{low} Tregs expressed both *Ccr4* and *Ccr8*, which are important for Treg and Th2 cell migration into the type-2 inflamed niche (*25–27*); notably, Gata3^{high} Tregs expressed more *Ccr8* transcript and surface protein compared to the other T cell subsets (Fig. 1G). Moreover, *Ccr7* expression was low on Gata3^{high} Tregs, while Gata3^{low} Tregs and Th2 cells expressed intermediate levels compared to Tconv cells; this may indicate a reduced ability of Gata3^{high} Tregs to traffic to the mediastinal lymph-node (medLN) via lymphatics. Furthermore, Gata3^{high} Tregs, Th2 cells and ILC2 all selectively expressed *Cxcr6*, which is associated with retention of lymphocytes in the tissue-niche (*28*). Thus, while all Treg and Th2 cells possess receptors to enter the type-2 inflamed lung niche, Gata3^{low} Tregs do not highly express genes required for retention in the lungs; conversely, Gata3^{high} Tregs (and Th2 cells to a lesser degree) possessed a stronger gene-signature related to tissue-residency (Fig. S1K).

We next performed TCR diversity analysis on the sorted T cell populations. We found that Gata3^{high} Tregs exhibited significantly reduced TCR diversity and increased proportions of hyper-expanded clones compared to Gata3^{low} Treg and Tconv cells (Fig. 1H, S1L). Interestingly, Th2 cells in IL-33-treated mice were clonally hyper-expanded, suggesting that endogenous Th2 cells expand in response

to local antigen or co-stimulation; indeed, both Gata3^{high} Treg and Th2 cells expressed higher levels of *Nr4a1* (Nur77), indicative of increased TCR stimulation (Fig. 1F).

To investigate how type-2 lymphocytes interact in the inflamed niche we performed *in silico* receptor-ligand interactome analysis using CellChat (*30*) (Fig. 1I, 1J, S1M and Table 1). Predicted heterotypic interactions were strongest between ILC2 and Tregs or Th2 cells. Interestingly, *Tnfsf4-Tnfrs4* was predicted to preferentially engage Gata3^{high} Tregs while also showing affinity for Gata3^{low} Treg and Th2 cells. Fitting with literature, ILC2 were predicted to engage in multiple autocrine interactions, including via Ccl1-Ccr8 signalling (*31*); our results also suggested that ILC2 preferentially engage Gata3^{high} Tregs via this interaction. We used *Ccr8$^{-/-}$* mice to test if this chemokine axis is important for the IL-33-driven expansion of Gata3^{high} Tregs. While Gata3^{high} Treg numbers were similar in both genotypes at rest, IL-33 administration resulted in impaired expansion of Gata3^{high} Tregs in *Ccr8$^{-/-}$* mice compared to wild-type control (Fig. 1K); notably, a diminished but significant effect of IL-33 in *Ccr8$^{-/-}$* mice suggested that other factors contributed. Moreover, the IL-33-driven increase in ILC2 and Gata3^{low} Treg numbers was not significantly affected by Ccr8 deficiency.

Lastly, we asked whether similar Treg subsets were present in human lungs using a publicly available single cell RNA-seq dataset of lung cancer patients (*31*) (Fig. S2A). Unsupervised clustering of *FOXP3^{+}* Tregs revealed 6 sub-clusters (Fig. S2B); notably, clusters 1, 4 and 6 expressed high *TNFRSF4, CCR8, CXCR6,* and *GATA3* transcripts, while clusters 2 and 3 were *GATA3^{low}* and expressed high *CCR7* (Fig. S2C), in agreement with our murine observations.

These data suggested that ILC2 serve as tissue-resident sentinels that can rapidly attract and engage Tregs after exposure to IL-33. Moreover, while chemokines are important, it is likely that other co-stimulatory ligand-receptor interactions contribute to the local expansion of Gata3^{high} Tregs.

ILC2 orchestrate IL-33-dependent expansion of tissue-resident Gata3^{high} Tregs in diverse anatomical sites.

IL-33 has a profound effect on the local expansion and maintenance of Tregs in different organs and tissues, however, it remains unclear if this is due to direct IL-33 signalling. To address this question, we generated mixed bone marrow chimeras using congenic *Il1rl1$^{-/-}$* and C57Bl/6 wild-type donors (Fig. 2A, S3A). Interestingly, we found no substantial effect on tissue-resident Treg numbers or proportions due to cell-intrinsic loss of the IL-33 receptor in many organs tested, including the lung, but also non-mucosal sites such as the pancreas and adipose tissue. Conversely, IL-33 administration resulted in the rapid expansion of Tregs in many peripheral sites (Fig. 2B). Notably, non-mucosal sites such as the pancreas also exhibited co-localisation of ILC2 and Tregs after IL-33 exposure, suggesting that IL-33-

responsive ILC2 may coordinate local Treg expansion (Fig. S3B). Like the lungs, IL-33 also induced the rapid and selective expansion of pancreatic Gata3^{high} Tregs, which preferentially expressed KLRG1 and were tissue-resident based on intravenous CD45.2 labelling experiments (Fig. S3C, S3D).

5   To ask if ILC2 are important mediators of local Treg expansion, we used ILC2-deficient $Il7r^{Cre/+}Rora^{fl/fl}$ or $Il7r^{Cre/+}$ control mice. Systemic administration of IL-33 induced the rapid expansion of Tregs in most anatomical sites of control mice, which was significantly impaired in ILC2-deficient animals (Fig. 2C). These results demonstrated that the effect of IL-33 on local Treg cell expansion in many anatomical sites <u>can be mediated</u> by ILC2.

10

It is known that co-stimulatory ligands can influence local ILC2-Treg cell interactions, including ICOSL and OX40L (20, 21). We therefore generated ICOSL- or used OX40L-conditional mutants where these co-stimulatory molecules were deleted on ILC2. Interestingly, IL-33 administration to $Il5^{Cre/+}Icosl^{fl/fl}$ or $Il5^{Cre/+}$ control mice resulted in similar expansion of Gata3^{high} Tregs in the airways, suggesting that

15   ICOSL-ICOS signalling was not essential (Fig. 2D). Conversely, $Il7r^{Cre/+}Tnfsf4^{fl/fl}$ mice showed a significant reduction in Gata3^{high} Treg expansion compared to $Il7r^{Cre/+}$ controls in the lung, as we previously reported (20), as well as in the pancreas, omentum and adipose tissue after IL-33 administration (Fig. 2D, S3E). <u>Gata3^{low} Treg numbers increased less compared to Gata3^{high} Tregs, and their expansion was not significantly affected in either $Il5^{Cre/+}Icosl^{fl/fl}$ or $Il7r^{Cre/+}Tnfsf4^{fl/fl}$ mice at this</u>

20   <u>time-point (Fig. S3F).</u> Moreover, OX40L expression was rapidly induced on lung ILC2 after IL-33 administration, and preceded the local expansion of Gata3^{high} Tregs, as demonstrated in a time-course experiment (Fig. 2E, S3G); we observed a similar induction of OX40L on ILC2 in other anatomical sites, including the pancreas (Fig. S3H). To profile cells for their ability to produce OX40L we used $Tnfsf4^{hCD4/+}$ reporter mice, where gene activity is measured instead of transient surface expression of

25   OX40L. We detected robust hCD4 expression on both lung and medLN ILC2 after IL-33 exposure, but none in PBS treated mice (Fig. 2F, 2G, S3I); moreover, we did not observe hCD4 expression on other lymphocytes, including lymph-node ILC3, at rest or after IL-33 administration (Fig. 2G). We next profiled $Tnfsf4^{hCD4/+}$ reporter mice for hCD4 expression on myeloid cells. We did not observe hCD4 expression by myeloid cell-types in PBS or IL-33 treated lungs, including alveolar or interstitial

30   macrophages, granulocytes, or dendritic cells (Fig. 2H). Notably, we observed some hCD4 expression by cDC2 in the medLN after IL-33 treatment (Fig. 2I). Altogether, these results suggest that the IL-33-ILC2-OX40L axis serves as an innate checkpoint for local Gata3^{high} Treg expansion.

Intrinsic OX40 signalling is required for IL-33-dependent Gata3^{high} Treg expansion.

35

To investigate if Treg-intrinsic OX40 signalling drove IL-33-mediated expansion we generated Treg-conditional mutants ($Foxp3^{Cre}Tnfrsf4^{fl/fl}$, OX40$^{\Delta Treg}$) that efficiently and specifically deleted OX40 on

Tregs (Fig. S4A). OX40$^{\Delta Treg}$ mice were born at Mendelian ratios and were phenotypically unremarkable compared to littermate controls. Detailed histological characterization of these mice revealed a minor increase in colonic immune infiltration (Fig. S4B, C). Nevertheless, the lungs of naïve PBS-treated OX40$^{\Delta Treg}$ mice were histologically similar to those of control mice (Fig. S5B).

5

Moreover, while total percentages of Tregs were slightly higher in the spleen, the number and percentage of Gata3^{high} Tregs were similar at baseline in the lungs and pancreata of OX40$^{\Delta Treg}$ compared to $Foxp3^{Cre}$ control mice, arguing against a substantial role for OX40 in tissue Treg maintenance (Fig. S4D). We performed *in vitro* suppression assays of flow-sorted splenic Tregs from $Foxp3^{Cre}$ control or OX40$^{\Delta Treg}$

10 mice, which showed that OX40-deletion did not impair their suppressive function (Fig. S4E). These results were reinforced by transcriptomic analysis of control and OX40-knockout Tregs, which showed that besides *Tnfrsf4*, the Treg transcriptome was largely unaffected at baseline, including Treg-associated transcription factors and surface molecules, including *Il1rl1* transcript (Fig. S4F-S4I), and surface ST2 expression (Fig. S4J).

15

Next, we treated OX40$^{\Delta Treg}$ or control mice with IL-33 or PBS followed by immune-phenotyping of different organs; IL-33-mediated expansion of Gata3^{high} Tregs was significantly reduced in the pancreas and spleen, while the proportion of Gata3^{high} Treg was substantially impaired in the pancreas, lung, and spleen (Fig. 2J, S4K). Hemizygous female $Foxp3^{YFP-Cre/+}Tnfrsf4^{fl/fl}$ mice were used to further control for

20 cell-extrinsic effects on IL-33-mediated Treg expansion (Fig. S4L); we found that YFP$^-$ OX40-sufficient Tregs expanded, while YFP$^+$ OX40-knockout Tregs failed to respond to IL-33 administration (Fig. S4M). Lastly, we generated $Foxp3^{CreERT2}Tnfrsf4^{fl/fl}$ mice to temporally delete OX40 on Tregs. Tamoxifen treatment before IL-33 administration resulted in efficient deletion of OX40, and significantly impaired Gata3^{high} Treg expansion in the lung and pancreas, similar to the constitutive knock-out (Fig. 2K, S4N).

25 In all, these data demonstrate a critical Treg cell-intrinsic role of OX40 for mediating IL-33-driven Gata3^{high} Treg expansion in diverse anatomical locations.

Treg-intrinsic OX40 is critical for the effective control of type-2 immunity.

30 As Treg-intrinsic loss of OX40 selectively impairs the expansion of Gata3^{high} Tregs, which efficiently restrain type-2 immunity (*8*), we hypothesized that OX40$^{\Delta Treg}$ mice would fail to control IL-33-driven type-2 pathologies. We intranasally sensitized and challenged OX40$^{\Delta Treg}$ and control mice with *Alternaria alternata* fungal allergen extract or PBS control on days 0, 1 and 14, followed by analysis for airway inflammation on day 20. While allergen exposure provoked a robust type-2 immune response

35 in control mice, OX40$^{\Delta Treg}$ mice experienced profound eosinophil-rich allergic lung inflammation (Fig. 3A, S5A). Moreover, we observed a significant increase in medLN eosinophil numbers in allergen challenged OX40$^{\Delta Treg}$ over control mice. Similarly, while sensitization and challenge induced effector

Gata3^{high} Th2 cell expansion in control mice, OX40$^{\Delta Treg}$ mice experienced a significant increase in numbers (Fig. 3B). Similarly, ILC2 numbers were increased in inflamed OX40$^{\Delta Treg}$ mice (Fig. 3C), although the fold increase in lung Th2 cells (33.9 fold) was higher than that of ILC2 (5.4 fold). Moreover, no significant or only minor changes were observed in alveolar macrophage and neutrophil numbers (Fig. 3D). Next, as a measure of lung function, we quantified breadth distention and blood oxygenation on three days following the last allergen challenge (Fig. 3E); while control mice experienced only minor changes in these parameters after allergen challenge, we observed a notable and persistent increase in breathing effort and reduced blood oxygenation in OX40$^{\Delta Treg}$ mice. Histological analysis of lungs on day 20 indicated that naïve mice of both genotypes did not exhibit inflammation, however allergen treated OX40$^{\Delta Treg}$ mouse lungs were substantially more inflamed compared to *Foxp3^{Cre}* control animals (Fig. 3F, S5B). We also assessed lung sections for mucins by periodic acid-Schiff stain and collagens by Trichrome stain, which both showed more intense staining in allergen treated OX40$^{\Delta Treg}$ mice (Fig. S5C, S5D). Next, we used the protease allergen papain as an alternative model of type-2 airway inflammation. Using a similar dosing scheme, we found that OX40$^{\Delta Treg}$ mice experienced significantly more type-2 inflammation, as assessed by quantification of lung ILC2 and Th2 cells and/or eosinophils in the lung, bronchoalveolar lavage and medLN (Fig. 3G). Moreover, bronchoalveolar lavage samples on day 20 were assessed for the eosinophil chemoattractant Ccl11 (Fig. 3H) which was significantly elevated in allergen treated OX40$^{\Delta Treg}$ mice. Similarly, we found that serum IgE concentrations were higher in OX40$^{\Delta Treg}$ mice compared to controls (Fig. 3I). Lastly, we performed intracellular staining for IL-5 as a measure of functional capacity of lung T cells or ILC after *in vitro* stimulation (Fig. S5E-I). We observed a significant increase in IL-5$^+$ Th2 cell numbers and percentage of CD4$^+$ T cells in OX40$^{\Delta Treg}$ compared to control mice after allergen stimulation but found no difference in their per-cell capacity to produce IL-5. As expected, ILC2 did not require allergen sensitization for IL-5 production when stimulated with PMA + ionomycin, and furthermore did not show differences between genotypes. Hence, we hypothesize that the increase in type-2 inflammation in OX40$^{\Delta Treg}$ mice is mainly driven by increased numbers of Th2 cells, although ILC2 may directly or indirectly contribute. In all, we conclude that OX40 expression by Tregs is critical for restraining airway type-2 inflammation after allergen exposure.

Allergen exposed OX40$^{\Delta Treg}$ mice have impaired Gata3^{high} Treg induction and uncontrolled effector memory Th2 cell expansion.

Inhaled allergens promote IL-33 release, which is essential for both ILC2 activation and subsequent Th2 cell responses (*32–35*). Given that this pathway also engages Gata3^{high} Tregs we assessed the lungs of *Foxp3^{Cre}* control and OX40$^{\Delta Treg}$ mice after *Alternaria alternata* challenge by flow cytometry (Fig. 4A, S6A). Gating on CD44$^+$CD62L$^-$ T cells, we find a significant enrichment of Gata3^{high} Tregs in control animals (Fig. 4B); concurrently, Gata3^{high} Treg proportions are significantly reduced in OX40$^{\Delta Treg}$

compared to control mice after allergen exposure. Conversely, the percentage of lung $CD44^+CD62L^-$ effector Th2 cells is significantly increased in $OX40^{\Delta Treg}$ mice (Fig. 4C). Notably, total leukocyte numbers are profoundly increased in allergen treated $OX40^{\Delta Treg}$ mice compared to control animals, resulting in overall increased Gata3^{low} and Gata3^{high} Treg numbers (Fig. S6B). However, when we compared the ratio of Th2 to Treg cells we observe that while control mice have constant ratios in naïve and inflamed lungs, $OX40^{\Delta Treg}$ mice failed to maintain an equilibrium, resulting in significantly higher effector Th2 to regulatory T cell proportions (Fig. 4D). We next used multiplex IF microscopy and HALO image analysis to determine the densities of ILC2, Treg and Th2 cells in the lungs of *Alternaria alternata* challenged *Foxp3^{Cre}* control and $OX40^{\Delta Treg}$ mice (Fig. 4E, 4F). Mirroring flow-cytometric data, we found that $OX40^{\Delta Treg}$ mouse lungs showed increased overall cell densities, and a marked increase in Th2 to Treg cell proportions compared to allergen-treated control mice (Fig. 4G). Moreover, like IL-33-treated lungs, we find that ILC2, Treg and Th2 cells localise near or within the adventitial cuff in *Alternaria alternata*-treated mice (Fig. S6C). Next, using the protease allergen papain, we also observed an impaired relative expansion of Gata3^{high} Tregs in $OX40^{\Delta Treg}$ mice and amplified Th2 cell expansion, resulting in significantly higher Th2 cell to Gata3^{high} Treg ratios in the lung (Fig. 4H-J, S6D). These data support our hypothesis that OX40-driven co-expansion of Tregs is important for the restraint of Th2 cell numbers during inflammation.

Given the importance of secondary lymphoid organs for generating both effector and memory Th2 cell responses, we next focussed our attention on the medLN (Fig. 4K). Unlike the lung, we did not observe significant changes in the proportion of Gata3^{high} or total Treg percentages after allergen challenge or between genotypes (Fig. 4L, S6E). However, the percentage of Th2 cells increased upon allergen challenge in control mice, and this was significantly amplified in $OX40^{\Delta Treg}$ mice (Fig. S6F). We then assessed Th2 cells for the presence of $CD44^+CD62L^-CD127^+$ effector memory cells (Fig. 4M) and found that allergen sensitized $OX40^{\Delta Treg}$ mice showed a significant increase in the percentage and absolute numbers of effector memory Th2 cells compared to control animals (Fig. 4N, 4O). Using papain allergen, we found a similar significant increase in the percentage of effector memory Th2 cells in the medLN of $OX40^{\Delta Treg}$ mice (Fig. 4P). Hence, we conclude that OX40 deficiency on Tregs results in a greatly amplified memory Th2 cell response in the lung-draining lymph node.

Gata3^{high} Tregs directly control OX40L availability and preferentially home to the inflamed lung.

Given the critical role of OX40L-OX40 signalling on the control of T cell memory (*36*), and ability of Tregs to control the surface expression of co-stimulatory ligands (*2*), we hypothesized that Tregs may modulate OX40L bioavailability on lung ILC2. Utilizing *Foxp3^{DTR}* mice, we asked if acute Treg depletion could influence OX40L expression upon IL-33 stimulation. Indeed, we observed a significant increase in the percentage and mean fluorescence intensity of OX40L on ILC2 in IL-33 plus diphtheria

toxin treated mice (Fig. 5A, 5B). Concomitant analysis of myeloid cell-types indicated that Treg depletion did not influence OX40L surface expression on granulocytes, or macrophage and dendritic cell subsets in IL-33 treated mice (Fig. 5C).

5   We next employed an *in vitro* co-culture system to assess the ability of Tregs to regulate OX40L expression on ILC2 (Fig. S7A). We used *Gata3^{YFP}Foxp3^{RFP}* mice to purify viable lung Gata3^{high} and Gata3^{low} Tregs, as well as Gata3^{high} ILC2 (Fig. 5D). Lung Treg subsets were able to suppress Tconv cells *in vitro*, confirming their conventional suppressive ability (Fig. S7B). Culture of ILC2 with IL-33 resulted in expression of OX40L, which was significantly reduced upon co-culture with Gata3^{high} Tregs,

10   while Gata3^{low} Tregs showed reduced capacity to suppress OX40L expression (Fig. 5E, 5F); conversely, co-culture with Tconv did not change OX40L expression on ILC2 (Fig. S7C). Importantly, we did not detect OX40L on the surface of Tregs *in vivo* after IL-33 administration or *in vitro* after co-culture with ILC2, arguing against trogocytosis-mediated suppression (Fig. 5A, 5E); moreover, we confirm that *Gata3* expression patterns were maintained by Tregs in culture (Fig. S7D).

15

We subsequently investigated the mechanism whereby Tregs modulate OX40L expression by ILC2. First, we found that *Tnfsf4* transcript levels were unchanged after co-culture with Tregs, arguing against transcriptional regulation (Fig. S7E). We also failed to detect soluble OX40L in co-cultures, suggesting that cleavage of membrane-bound receptors did not account for loss of expression (*data not shown*);

20   relatedly, blocking ADAM proteases did not affect Treg-mediated suppression of OX40L on ILC2 (Fig. S7C). Next, we focussed on internalization of OX40L; however, we found that while blocking endocytosis using Pitstop-2 increased OX40L surface expression on ILC2 in monocultures, the addition of this reagent did not impact Treg-dependent reductions of OX40L expression in co-culture (Fig. 5G). Interestingly, the addition of recombinant IL-10 or TGF-β1 to ILC2 monocultures resulted in a

25   significant reduction in OX40L surface expression; however, blockade of either single or both suppressive molecules in ILC2-Treg co-cultures did not revert suppression of OX40L (Fig. 5G). Notably, recombinant IL-10 and TGF-β influenced *Tnfsf4* transcript level (Fig. S7E), indicating a different mechanism of control. Moreover, we sorted Tregs from OX40^{ΔTreg} mouse lungs which were able, but less-effective than Gata3^{high} Tregs at suppressing OX40L on ILC2 (Fig. 5H); while reduced

30   Gata3^{high} Treg numbers in OX40^{ΔTreg} mouse lungs likely contributed to this result, it also demonstrated that the regulation of OX40L on ILC2 could occur independently of receptor-ligand engagement. This finding was further substantiated using anti-OX40 mAb in co-cultures, which did not affect OX40L suppression by Tregs (Fig. 5G).

35   We used computational tools to explore alternative regulatory mechanisms. First, we analysed predicted Treg-to-ILC2 communication, focussing on modules enriched in Gata3^{high} Tregs (Fig. 5I, 5J, Table 2). These included adhesion molecules (*Vcam1*, *Icam1*, *Lamc1*, and *Lgals9*) and the ATP hydrolase CD39

(*Entpd1*), amongst others. Interestingly, IL-10 and TGF-β signalling pathways were not predicted, although this matched our *in vitro* results, and may reflect the lack of TCR stimulation of the Tregs in our setting. Notably, our previous ILC2-to-Treg communication analysis also identified ICOSL-ICOS interactions (Table 1); while these were not important for mediating Treg expansion, ICOS signalling is known to enhance Treg function (*37*). We also compared relative gene expression of known or putative regulatory mechanisms employed by Tregs in our dataset (Fig. 5K). Besides the secreted factors already investigated, we found that Gata3high Tregs expressed *Fgl2*, although this was also highly expressed by ILC2 themselves, as well as *Ebi3* which together with *Il12a* forms IL-35. In terms of inhibitory surface molecules *Pdcd1lg2* (PD-L2) was highly expressed by both Gata3high Tregs and ILC2, while the soluble or membrane molecule *Cd83* (CD83) was selective for the former. Gata3high Tregs also selectively expressed *Il2ra*, *Il1r2* and *Il1rl1*, which may act to inhibit IL-2 or IL-33 signalling. Lastly, surface enzymes including *Entpd1* and *Nt5e* (CD73) were expressed by Gata3high Tregs, indicating that adenosine mediated signalling could contribute to reduced OX40L expression by ILC2. Extending on the computational predictions, we observed that ICOSL was expressed by ILC2 *in vitro* (Fig. S7F); moreover, blocking ICOSL in co-cultures resulted in a moderate increase of OX40L on ILC2 (Fig. 5L). Similarly, ICAM-1 blocking mAb in co-cultures resulted in a partial rescue of OX40L expression on ILC2 (Fig. 5M). However, blocking PD-1 or components of the adenosine pathway using a CD37 inhibitor (POM-1) or Adora2a antagonist (A2ARi) in co-cultures had no effect on OX40L expression (Fig. 5L-N). Hence, multifaceted two-way dialogue between ILC2 and Tregs appears to coordinate the suppressive function of the latter.

Lastly, as ILC2-Treg co-localisation likely underpins their regulatory function, we asked if Gata3high Tregs preferentially home to the inflamed lung. We adoptively transferred equal numbers of lung Gata3high and Gata3low Tregs into IL-33-treated *Rag2*-/- recipient mice, which lack T and B cells but have lung ILC2, followed by quantification of Tregs in the lungs and spleen (Fig. 5O, S7G). We observed significantly more Gata3high Tregs in the lung, while equal but greatly reduced numbers of Gata3high and Gata3low Tregs were recovered in the spleen. Moreover, we find that adoptively transferred Tregs maintained their *Gata3* expression pattern (Fig. S7H). In summary these data showed that airway Gata3high Tregs are endowed to traffic to the inflamed lung niche, while also possessing enhanced capacity for regulating OX40L expression on ILC2.

OX40+ Tregs control adaptive type-2 immunity by modulating OX40L availability.

Our data advance a paradigm whereby OX40-expression on Tregs is important for their local expansion and modulation of OX40L expression by ILC2. Indeed, we found that OX40L expression by ILC2 was enhanced in OX40ΔTreg mice after administration of papain protease allergen (Fig. S8A). Increased OX40L availability in the absence of efficient regulation by Gata3high Tregs may therefore explain the

unrestrained effector memory Th2 cell formation in OX40$^{\Delta Treg}$ mice. To test this hypothesis, we used two approaches; first we asked if we could restore Th2 cell-driven allergic inflammation in OX40L$^{\Delta ILC2}$ mice using an OX40 agonist (Fig. S8B). As expected, OX40L$^{\Delta ILC2}$ mice failed to mount an efficient Th2 cell response to inhaled allergen papain (Fig. 6A). Agonistic murine IgG1 anti-OX40 administration led to the restoration of both airway Th2 cell responses and increased type-2 inflammation, while also promoting a trend towards more Gata3^{high} Tregs. In the medLN, OX40-agonist treatment reversed a significant defect in effector memory Th2 cell formation observed in OX40L$^{\Delta ILC2}$ mice and rescued the absolute numbers of Th2 cells (Fig. 6B).

Next, we asked if increased OX40L availability was responsible for unrestrained Th2 cell-driven inflammation by neutralizing OX40L in OX40$^{\Delta Treg}$ mice (Fig. S8C). As expected, OX40$^{\Delta Treg}$ mice treated with papain allergen exhibited amplified type-2 airway inflammation and Th2 cell numbers, while Gata3^{high} Treg expansion was impaired (Fig. 6C); anti-OX40L treatment of OX40$^{\Delta Treg}$ mice significantly reduced type-2 inflammation and airway Th2 cell numbers. Notably, we found no additive effect of OX40L-neutralization on Gata3^{high} Treg enrichment in OX40$^{\Delta Treg}$ mice. More strikingly, we found that OX40L neutralization reverted the amplified CD127$^+$ effector memory Th2 cell phenotype observed in the medLN of OX40$^{\Delta Treg}$ mice (Fig. 6D, 6E), which resulted in significant reductions in effector memory Th2 cell percentages and numbers, and an overall reduction in Th2 cells (Fig. 6E). Histological analysis of the lungs further indicated that overt allergic inflammation observed in OX40$^{\Delta Treg}$ mice after allergen exposure was reduced by anti-OX40L treatment (Fig. 6F). Lastly, we leveraged 2W1S peptide-specific tetramers to better understand the effect of Treg-derived OX40, and OX40L-neutralization, on the clonal dynamics of Th2 cells. Papain plus 2W1S peptide administration resulted in the expansion of 2W1S:tetramer$^+$ CD4$^+$ T cells, which were skewed towards a Gata3$^+$ Th2 cell fate (Fig. 6G). Mirroring total Th2 cell results, we found that OX40$^{\Delta Treg}$ mice treated with papain plus 2W1S peptide had significantly more 2W1S:tetramer$^+$ Th2 cells, which were reduced with neutralization of OX40L (Fig. 6G). Overall, these data support our hypothesis that OX40L availability is tuned by OX40$^+$ regulatory T cells; this mechanism controls the magnitude of adaptive type-2 immunity by regulating immune memory formation.

Discussion

Local immune-regulatory mechanisms are fundamentally important for maintaining or restoring tissue-homeostasis. Our data advance a paradigm whereby innate lymphoid cells are critical immune-regulatory hubs that establish local immune tolerance or immune restraint; specifically, we show that Treg-mediated control of adaptive type-2 immunity is contingent on direct dialogue with ILC2 (Figure 6H). While ILC2-Treg interactions are multifaceted, OX40L-OX40 signalling was of prime importance, and served as a crucial innate immune checkpoint for the local expansion of Gata3^{high} Tregs; this Treg

subset could efficiently exert feedback control on the local bioavailability of OX40L on ILC2, which profoundly influenced effector memory Th2 cell densities and the magnitude of type-2 inflammation.

While ILC2 are emerging as drivers of adaptive type-2 immunity (*38*), their ability to restrain type-2 inflammation remains unclear. ILC-intrinsic regulatory functions are also reported (*39–41*), although these do not compensate for the loss of Treg expansion on increased type-2 inflammation in OX40$^{\Delta Treg}$ mice. Relatedly, we do not observe a substantial transcriptomic ILC2$_{10}$ signature (*39, 42–44*) at the time-point where we observe OX40L expression by ILC2, although it is possible that IL-10 is produced by ILC2 subsequently; notably, ILC2$_{10}$ are reported to emerge after chronic ILC2 stimulation (*45*).

In terms of their regulatory function, we argue that ILC2 maintain local parity between Treg and Th2 cell numbers upon induction of inflammation; this ability to locally coordinate cells is multi-layered and involves chemotaxis and co-stimulatory interactions, amongst other predicted mechanisms. Interestingly, we found that ICOSL-ICOS signalling was important for Treg function, but not IL-33-driven expansion; these and our OX40L-OX40 data reconcile previous findings (*20, 21*), but also raise questions about how these molecules control Treg biology in other types of inflammation. Similarly, ICAM-1 mediates Treg function (*46*), and contributes to controlling OX40L expression on ILC2. Conversely, we found that other known immunosuppressive mechanisms, including TGF-β, IL-10, and adenosine-mediated signalling were not involved. Moreover, high *Il1rl1* (ST2) expression by Gata3^{high} Tregs could act as an IL-33 sink, thereby influencing ILC2 function; we also find that lung Gata3^{high} Tregs are functional in standard T cell suppression assays, indicating that direct regulatory mechanism may contribute to their role in controlling type-2 inflammation. These *in vitro* and *in silico* findings provide a foundation for future investigations into tissue-localised regulatory mechanisms of Tregs.

Relatedly, the relative contribution of ILC2 and Th2 cells in driving overall type-2 inflammation after allergen challenge remains incompletely understood. While CD4 T cells are critical mediators of the antigen-recall response, and the profound increase in type-2 inflammation in OX40$^{\Delta Treg}$ mice, we also observe a significant increase in ILC2 numbers over allergen-stimulated control mice. This might be explained by the synergistic effect of T cell-derived factors on ILC2 expansion (*47*).

Group 3 innate lymphoid cells (ILC3) can also express OX40L in the intestines, although direct antigen-presentation by ILC3 appears to dominate their interaction with gut Tregs (*48, 49*). We also highlight the unappreciated and divergent effect of the OX40L-OX40 dyad on both the effector and regulatory arms of type-2 immunity, and that ILC2 are positioned centrally in this cellular circuit. Notably, ILC2 are the primary source of OX40L in our inflammatory model, but the role of other OX40L expressing cell-types should be assessed (*50*). Interestingly, Tregs can modulate OX40L on DC via trogocytosis (*51*), although we do not find evidence of this process with ILC2. Nevertheless, the ability of Tregs to

modulate OX40L bioavailability on ILC2 fits with our general understanding of how Tregs can locally control mitogen levels. Given the broad and generally untargeted therapeutic exploitation of OX40, our findings may stimulate more refined targeting of either effector or regulatory arms of this pathway.

5   The ability of Tregs to function depends largely on how they are locally coordinated, and, befitting an emerging framework of inflammation-tailored Treg subsets, we find that Gata3^{high} Tregs preferentially engage ILC2 in the type-2 inflamed niche. Nevertheless, Gata3 is constitutively expressed by all Tregs and enforces the maintenance and function of Foxp3 (*52*), while Gata3^{high} Tregs upregulate both known and potentially unappreciated target genes that affect their adaptation to the type-2 niche (*53*, *54*).

10 Moreover, while Gata3^{low} Tregs, which also express lower *Tnfrsf4*, are not preferentially enriched in the type-2 inflamed nice, their expansion is also affected in ILC2-deficient mice. Hence, it is likely that other factors of the type-2 niche collaborate to attract Tregs, including ILC2-activated dendritic cells that secrete the type-2 chemokines CCL17 and CCL22 (*33*, *55*), or extracellular matrix components such as hyaluronic acid, which binds to CD44 that is highly expressed on Gata3^{high} Tregs (*56*). Regarding

15 Treg function, we demonstrate their role in a critical checkpoint on the size of the Th2 effector memory cell compartment that depended on OX40 expression, and local interactions with ILC2. Whether this cellular mechanism operates in other diseases is unknown, although our analysis of published single cell data indicates that similar *GATA3^{high}* Tregs are also present in lung cancer patients. In all, this work reveals critical cellular circuitry that underpins Treg-mediated control of adaptive type-2 immunity.

20

Materials and methods

See Supplementary Materials

List of supplementary materials

25 Materials and Methods

Supplemental Figure 1-8

Supplemental Table 1 and 2

References

1. M. L. Meizlish, R. A. Franklin, X. Zhou, R. Medzhitov, Tissue Homeostasis and Inflammation. *Annu. Rev. Immunol.* **39**, 557–581 (2021).

2. S. Dikiy, A. Y. Rudensky, Principles of regulatory T cell function. *Immunity* **56**, 240–255 (2023).

3. B. R. Powell, N. R. M. Buist, P. Stenzel, An X-linked syndrome of diarrhea, polyendocrinopathy, and fatal infection in infancy. *J. Pediatr.* **100**, 731–737 (1982).

4. K. Lahl, C. T. Mayer, T. Bopp, J. Huehn, C. Loddenkemper, G. Eberl, G. Wirnsberger, K. Dornmair, R. Geffers, E. Schmitt, J. Buer, T. Sparwasser, Nonfunctional regulatory T cells and defective control of Th2 cytokine production in natural scurfy mutant mice. *J. Immunol.* **183**, 5662–5672 (2009).

5. T. A. Chatila, F. Blaeser, N. Ho, H. M. Lederman, C. Voulgaropoulos, C. Helms, A. M. Bowcock, JM2, encoding a fork head-related protein, is mutated in X-linked autoimmunity-allergic disregulation syndrome. *J. Clin. Invest.* **106**, R75-81 (2000).

6. Y. Zheng, A. Chaudhry, A. Kas, P. deRoos, J. M. Kim, T.-T. Chu, L. Corcoran, P. Treuting, U. Klein, A. Y. Rudensky, Regulatory T-cell suppressor program co-opts transcription factor IRF4 to control T(H)2 responses. *Nature* **458**, 351–356 (2009).

7. E. A. Wohlfert, J. R. Grainger, N. Bouladoux, J. E. Konkel, G. Oldenhove, C. H. Ribeiro, J. A. Hall, R. Yagi, S. Naik, R. Bhairavabhotla, W. E. Paul, R. Bosselut, G. Wei, K. Zhao, M. Oukka, J. Zhu, Y. Belkaid, GATA3 controls Foxp3$^+$ regulatory T cell fate during inflammation in mice. *J. Clin. Invest.* **121**, 4503–4515 (2011).

8. Y. Wang, M. A. Su, Y. Y. Wan, An essential role of the transcription factor GATA-3 for the function of regulatory T cells. *Immunity* **35**, 337–348 (2011).

9. M. A. Koch, G. Tucker-Heard, N. R. Perdue, J. R. Killebrew, K. B. Urdahl, D. J. Campbell, The transcription factor T-bet controls regulatory T cell homeostasis and function during type 1 inflammation. *Nat. Immunol.* **10**, 595–602 (2009).

10. D. R. Littman, A. Y. Rudensky, Th17 and regulatory T cells in mediating and restraining inflammation. *Cell* **140**, 845–858 (2010).

11. J.-E. Turner, H.-J. Paust, O. M. Steinmetz, A. Peters, J.-H. Riedel, A. Erhardt, C. Wegscheid, J. Velden, S. Fehr, H.-W. Mittrücker, G. Tiegs, R. A. K. Stahl, U. Panzer, CCR6 recruits regulatory T cells and Th17 cells to the kidney in glomerulonephritis. *J. Am. Soc. Nephrol.* **21**, 974–985 (2010).

12. R. Singh, D. Alape, A. de Lima, J. Ascanio, A. Majid, S. P. Gangadharan, Regulatory T Cells in Respiratory Health and Diseases. *Pulm. Med.* **2019**, 1907807 (2019).

13. P. Bacher, F. Heinrich, U. Stervbo, M. Nienen, M. Vahldieck, C. Iwert, K. Vogt, J. Kollet, N. Babel, B. Sawitzki, C. Schwarz, S. Bereswill, M. M. Heimesaat, G. Heine, G. Gadermaier, C. Asam, M. Assenmacher, O. Kniemeyer, A. A. Brakhage, F. Ferreira, M. Wallner, M. Worm, A. Scheffold, Regulatory T Cell Specificity Directs Tolerance versus Allergy against Aeroantigens in Humans. *Cell* **167**, 1067-1078.e16 (2016).

14. P. Bacher, A. Scheffold, The effect of regulatory T cells on tolerance to airborne allergens and allergen immunotherapy. *J. Allergy Clin. Immunol.* **142**, 1697–1709 (2018).

15. C. Schiering, T. Krausgruber, A. Chomka, A. Fröhlich, K. Adelmann, E. A. Wohlfert, J. Pott, T. Griseri, J. Bollrath, A. N. Hegazy, O. J. Harrison, B. M. J. Owens, M. Löhning, Y. Belkaid, P. G. Fallon, F. Powrie, The alarmin IL-33 promotes regulatory T-cell function in the intestine. *Nature* **513**, 564–568 (2014).

16. L. D. Faustino, J. W. Griffith, R. A. Rahimi, K. Nepal, D. L. Hamilos, J. L. Cho, B. D. Medoff, J. J. Moon, D. A. A. Vignali, A. D. Luster, Interleukin-33 activates regulatory T cells to suppress innate γδ T cell responses in the lung. *Nat. Immunol.* **21**, 1371–1383 (2020).

17. D. Kolodin, N. van Panhuys, C. Li, A. M. Magnuson, D. Cipolletta, C. M. Miller, A. Wagers, R. N. Germain, C. Benoist, D. Mathis, Antigen- and cytokine-driven accumulation of regulatory T cells in visceral adipose tissue of lean mice. *Cell Metab.* **21**, 543–557 (2015).

18. A. Vasanthakumar, K. Moro, A. Xin, Y. Liao, R. Gloury, S. Kawamoto, S. Fagarasan, L. A. Mielke, S. Afshar-Sterle, S. L. Masters, S. Nakae, H. Saito, J. M. Wentworth, P. Li, W. Liao, W. J. Leonard, G. K. Smyth, W. Shi, S. L. Nutt, S. Koyasu, A. Kallies, The transcriptional regulators IRF4, BATF and IL-33 orchestrate development and maintenance of adipose tissue–resident regulatory T cells. *Nat. Immunol.* **16**, 276–285 (2015).

19. W. Kuswanto, D. Burzyn, M. Panduro, K. K. Wang, Y. C. Jang, A. J. Wagers, C. Benoist, D. Mathis, Poor Repair of Skeletal Muscle in Aging Mice Reflects a Defect in Local, Interleukin-33-Dependent Accumulation of Regulatory T Cells. *Immunity* **44**, 355–367 (2016).

20. T. Y. F. Halim, B. M. J. Rana, J. A. Walker, B. Kerscher, M. D. Knolle, H. E. Jolin, E. M. Serrao, L. Haim-Vilmovsky, S. A. Teichmann, H.-R. Rodewald, M. Botto, T. J. Vyse, P. G. Fallon, Z. Li, D. R. Withers, A. N. J. McKenzie, Tissue-Restricted Adaptive Type 2 Immunity Is Orchestrated by Expression of the Costimulatory Molecule OX40L on Group 2 Innate Lymphoid Cells. *Immunity* **48**, 1195-1207.e6 (2018).

21. A. B. Molofsky, F. Van Gool, H.-E. Liang, S. J. Van Dyken, J. C. Nussbaum, J. Lee, J. A. Bluestone, R. M. Locksley, Interleukin-33 and Interferon-γ Counter-Regulate Group 2 Innate Lymphoid Cell Activation during Immune Perturbation. *Immunity* **43**, 161–174 (2015).

22. S. Hemmers, M. Schizas, A. Y. Rudensky, T reg cell-intrinsic requirements for ST2 signaling in health and neuroinflammation. *J. Exp. Med.* **218** (2021).

23. M. W. Dahlgren, S. W. Jones, K. M. Cautivo, A. Dubinin, J. F. Ortiz-Carpena, S. Farhat, K. S. Yu, K. Lee, C. Wang, A. V. Molofsky, A. D. Tward, M. F. Krummel, T. Peng, A. B. Molofsky, Adventitial Stromal Cells Define Group 2 Innate Lymphoid Cell Tissue Niches. *Immunity* **50**, 707-722.e6 (2019).

24. T. N. Rao, S. Kumar, A. J. Pulikkottil, F. Oliveri, R. W. Hendriks, F. Beckel, H. J. Fehling, Novel, Non-Gene-Destructive Knock-In Reporter Mice Refute the Concept of Monoallelic Gata3 Expression. *J. Immunol.* **204**, 2600–2611 (2020).

25. L. Faustino, D. Mucida, A. C. Keller, J. Demengeot, K. Bortoluci, L. R. Sardinha, M. Carla Takenaka, A. S. Basso, A. M. C. Faria, M. Russo, Regulatory T cells accumulate in the lung allergic inflammation and efficiently suppress T-cell proliferation but not Th2 cytokine production. *Clin. Dev. Immunol.* **2012**, 721817 (2012).

26. Z. Mikhak, M. Fukui, A. Farsidjani, B. D. Medoff, A. M. Tager, A. D. Luster, Contribution of CCR4 and CCR8 to antigen-specific T(H)2 cell trafficking in allergic pulmonary inflammation. *J. Allergy Clin. Immunol.* **123**, 67-73.e3 (2009).

27. B. D. Sather, P. Treuting, N. Perdue, M. Miazgowicz, J. D. Fontenot, A. Y. Rudensky, D. J. Campbell, Altering the distribution of Foxp3+ regulatory T cells results in tissue-specific inflammatory disease. *J. Exp. Med.* **204**, 1335–1347 (2007).

28. K. Obata-Ninomiya, K. Ishiwata, H. Nakano, Y. Endo, T. Ichikawa, A. Onodera, K. Hirahara, Y. Okamoto, H. Kanuka, T. Nakayama, CXCR6+ST2+ memory T helper 2 cells induced the expression of major basic protein in eosinophils to reduce the fecundity of helminth. *Proceedings of the National Academy of Sciences* **115**, E9849–E9858 (2018).

29. S. Jin, C. F. Guerrero-Juarez, L. Zhang, I. Chang, R. Ramos, C.-H. Kuan, P. Myung, M. V. Plikus, Q. Nie, Inference and analysis of cell-cell communication using CellChat. *Nat. Commun.* **12**, 1–20 (2021).

30. L. Knipfer, A. Schulz-Kuhnt, M. Kindermann, V. Greif, C. Symowski, D. Voehringer, M. F. Neurath, I. Atreya, S. Wirtz, A CCL1/CCR8-dependent feed-forward mechanism drives ILC2 functions in type 2-mediated inflammation. *J. Exp. Med.* **216**, 2763–2777 (2019).

31. A. G. Dykema, J. Zhang, L. S. Cheung, S. Connor, B. Zhang, Z. Zeng, C. M. Cherry, T. Li, J. X. Caushi, M. Nishimoto, A. J. Munoz, Z. Ji, W. Hou, W. Zhan, D. Singh, T. Zhang, R. Rashid, M. Mitchell-Flack, S. Bom, A. Tam, N. Ionta, T. H. K. Aye, Y. Wang, C. A. Sawosik, L. E. Tirado, L. M. Tomasovic, D. VanDyke, J. B. Spangler, V. Anagnostou, S. Yang, J. Spicer, R. Rayes, J. Taube, J. R. Brahmer, P. M. Forde, S. Yegnasubramanian, H. Ji, D. M. Pardoll, K. N. Smith, Lung tumor-infiltrating Treg have divergent transcriptional profiles and function linked to checkpoint blockade response. *Sci Immunol* **8**, eadg1487 (2023).

32. S. J. Van Dyken, J. C. Nussbaum, J. Lee, A. B. Molofsky, H.-E. Liang, J. L. Pollack, R. E. Gate, G. E. Haliburton, C. J. Ye, A. Marson, D. J. Erle, R. M. Locksley, A tissue checkpoint regulates type 2 immunity. *Nat. Immunol.* **17**, 1381–1387 (2016).

33. T. Y. F. Halim, Y. Y. Hwang, S. T. Scanlon, H. Zaghouani, N. Garbi, P. G. Fallon, A. N. J. McKenzie, Group 2 innate lymphoid cells license dendritic cells to potentiate memory TH2 cell responses. *Nat. Immunol.* **17**, 57–64 (2016).

34. T. Y. F. Halim, R. H. Krauss, A. C. Sun, F. Takei, Lung natural helper cells are a critical source of Th2 cell-type cytokines in protease allergen-induced airway inflammation. *Immunity* **36**, 451–463 (2012).

35. C. Cayrol, A. Duval, P. Schmitt, S. Roga, M. Camus, A. Stella, O. Burlet-Schiltz, A. Gonzalez-de-Peredo, J.-P. Girard, Environmental allergens induce allergic inflammation through proteolytic maturation of IL-33. *Nat. Immunol.* **19**, 375–385 (2018).

36. I. Gramaglia, A. Jember, S. D. Pippig, A. D. Weinberg, N. Killeen, M. Croft, The OX40 costimulatory receptor determines the development of CD4 memory by regulating primary clonal expansion. *J. Immunol.* **165**, 3043–3050 (2000).

37. D. Rigas, G. Lewis, J. L. Aron, B. Wang, H. Banie, I. Sankaranarayanan, L. Galle-Treger, H. Maazi, R. Lo, G. J. Freeman, A. H. Sharpe, P. Soroosh, O. Akbari, Type 2 innate lymphoid cell suppression by regulatory T cells attenuates airway hyperreactivity and requires inducible T-cell costimulator–inducible T-cell costimulator ligand interaction. *J. Allergy Clin. Immunol.* **139**, 1468-1477.e2 (2017).

38. M. J. Schuijs, T. Y. F. Halim, Group 2 innate lymphocytes at the interface between innate and adaptive immunity. *Ann. N. Y. Acad. Sci.* **1417**, 87–103 (2018).

39. C. R. Seehus, A. Kadavallore, B. de la Torre, A. R. Yeckes, Y. Wang, J. Tang, J. Kaye, Alternative activation generates IL-10 producing type 2 innate lymphoid cells. *Nat. Commun.* **8**, 1900 (2017).

40. S. Q. Crome, L. T. Nguyen, S. Lopez-Verges, S. Y. C. Yang, B. Martin, J. Y. Yam, D. J. Johnson, J. Nie, M. Pniak, P. H. Yen, A. Milea, R. Sowamber, S. R. Katz, M. Q. Bernardini, B. A. Clarke, P. A. Shaw, P. A. Lang, H. K. Berman, T. J. Pugh, L. L. Lanier, P. S. Ohashi, A distinct innate lymphoid cell population regulates tumor-associated T cells. *Nat. Med.* **23**, 368–375 (2017).

41. S. Wang, P. Xia, Y. Chen, Y. Qu, Z. Xiong, B. Ye, Y. Du, Y. Tian, Z. Yin, Z. Xu, Z. Fan, Regulatory Innate Lymphoid Cells Control Innate Intestinal Inflammation. *Cell* **171**, 201-216.e18 (2017).

42. E. Howard, G. Lewis, L. Galle-Treger, B. P. Hurrell, D. G. Helou, P. Shafiei-Jahani, J. D. Painter, G. A. Muench, P. Soroosh, O. Akbari, IL-10 production by ILC2s requires Blimp-1 and cMaf, modulates cellular metabolism, and ameliorates airway hyperreactivity. *J. Allergy Clin. Immunol.* **147**, 1281-1295.e5 (2021).

43. J. K. Bando, S. Gilfillan, B. Di Luccia, J. L. Fachi, C. Sécca, M. Cella, M. Colonna, ILC2s are the predominant source of intestinal ILC-derived IL-10. *J. Exp. Med.* **217** (2020).

44. H. Morita, T. Kubo, B. Rückert, A. Ravindran, M. B. Soyka, A. O. Rinaldi, K. Sugita, M. Wawrzyniak, P. Wawrzyniak, K. Motomura, M. Tamari, K. Orimo, N. Okada, K. Arae, K. Saito, C. Altunbulakli, F. Castro-Giner, G. Tan, A. Neumann, K. Sudo, L. O'Mahony, K. Honda, S. Nakae, H. Saito, J. Mjösberg, G. Nilsson, K. Matsumoto, M. Akdis, C. A. Akdis, Induction of human regulatory innate lymphoid cells from group 2 innate lymphoid cells by retinoic acid. *J. Allergy Clin. Immunol.* **143**, 2190-2201.e9 (2019).

45. C. Miyamoto, S. Kojo, M. Yamashita, K. Moro, G. Lacaud, K. Shiroguchi, I. Taniuchi, T. Ebihara, Runx/Cbfβ complexes protect group 2 innate lymphoid cells from exhausted-like hyporesponsiveness during allergic airway inflammation. *Nat. Commun.* **10**, 1–13 (2019).

46. G. Gottrand, T. Courau, V. Thomas-Vaslin, N. Prevel, T. Vazquez, M. G. Ruocco, B. Lambrecht, B. Bellier, B. M. Colombo, D. Klatzmann, Regulatory T-cell development and function are impaired in mice lacking membrane expression of full length intercellular adhesion molecule-1. *Immunology* **146**, 657–670 (2015).

47. C. J. Oliphant, Y. Y. Hwang, J. A. Walker, M. Salimi, S. H. Wong, J. M. Brewer, A. Englezakis, J. L. Barlow, E. Hams, S. T. Scanlon, G. S. Ogg, P. G. Fallon, A. N. J. McKenzie, MHCII-mediated dialog between group 2 innate lymphoid cells and CD4(+) T cells potentiates type 2 immunity and promotes parasitic helminth expulsion. *Immunity* **41**, 283–295 (2014).

48. M. Lyu, H. Suzuki, L. Kang, F. Gaspal, W. Zhou, J. Goc, L. Zhou, J. Zhou, W. Zhang, Z. Shen, J. G. Fox, R. E. Sockolow, T. M. Laufer, Y. Fan, G. Eberl, D. R. Withers, G. F. Sonnenberg, ILC3s select microbiota-specific regulatory T cells to establish tolerance in the gut. *Nature* **610**, 744–751 (2022).

49. T. Deng, C. Suo, J. Chang, R. Yang, J. Li, T. Cai, J. Qiu, ILC3-derived OX40L is essential for homeostasis of intestinal Tregs in immunodeficient mice. *Cell. Mol. Immunol.* **17**, 163–177 (2020).

50. M. Croft, Control of Immunity by the TNFR-Related Molecule OX40 (CD134). *Annu. Rev. Immunol.* **28**, 57–78 (2010).

51. H. Iriki, H. Takahashi, N. Wada, H. Nomura, M. Mukai, A. Kamata, H. Ito, J. Yamagami, T. Matsui, Y. Kurebayashi, S. Mise-Omata, H. Nishimasu, O. Nureki, A. Yoshimura, S. Hori, M. Amagai, Peripheral tolerance by Treg via constraining OX40 signal in autoreactive T cells against desmoglein 3, a target antigen in pemphigus. *Proc. Natl. Acad. Sci. U. S. A.* **118** (2021).

52. D. Rudra, P. deRoos, A. Chaudhry, R. E. Niec, A. Arvey, R. M. Samstein, C. Leslie, S. A. Shaffer, D. R. Goodlett, A. Y. Rudensky, Transcription factor Foxp3 and its protein partners form a complex regulatory network. *Nat. Immunol.* **13**, 1010–1019 (2012).

53. T. Nakayama, K. Hieshima, T. Arao, Z. Jin, D. Nagakubo, A.-K. Shirakawa, Y. Yamada, M. Fujii, N. Oiso, A. Kawada, K. Nishio, O. Yoshie, Aberrant expression of Fra-2 promotes CCR4 expression and cell proliferation in adult T-cell leukemia. *Oncogene* **27**, 3221–3232 (2008).

54. L. Guo, G. Wei, J. Zhu, W. Liao, W. J. Leonard, K. Zhao, W. Paul, IL-1 family members and STAT activators induce cytokine production by Th2, Th17, and Th1 cells. *Proc. Natl. Acad. Sci. U. S. A.* **106**, 13463–13468 (2009).

55. L. Halim, M. Romano, R. McGregor, I. Correa, P. Pavlidis, N. Grageda, S.-J. Hoong, M. Yuksel, W. Jassem, R. F. Hannen, M. Ong, O. Mckinney, B. Hayee, S. N. Karagiannis, N. Powell, R. I. Lechler, E. Nova-Lamperti, G. Lombardi, An Atlas of Human Regulatory T Helper-like Cells Reveals Features of Th2-like Tregs that Support a Tumorigenic Environment. *Cell Rep.* **20**, 757–770 (2017).

56. M. Firan, S. Dhillon, P. Estess, M. H. Siegelman, Suppressor activity and potency among regulatory T cells is discriminated by functionally active CD44. *Blood* **107**, 619–627 (2006).

57. J. M. Kim, J. P. Rasmussen, A. Y. Rudensky, Regulatory T cells prevent catastrophic autoimmunity throughout the lifespan of mice. *Nat. Immunol.* **8**, 191–197 (2007).

58. Y. P. Rubtsov, J. P. Rasmussen, E. Y. Chi, J. Fontenot, L. Castelli, X. Ye, P. Treuting, L. Siewe, A. Roers, W. R. Henderson Jr, W. Muller, A. Y. Rudensky, Regulatory T cell-derived interleukin-10 limits inflammation at environmental interfaces. *Immunity* **28**, 546–558 (2008).

59. Y. P. Rubtsov, R. E. Niec, S. Josefowicz, L. Li, J. Darce, D. Mathis, C. Benoist, A. Y. Rudensky, Stability of the regulatory T cell lineage in vivo. *Science* **329**, 1667–1671 (2010).

60. Y. Y. Wan, R. A. Flavell, Identifying Foxp3-expressing suppressor T cells with a bicistronic reporter. *Proc. Natl. Acad. Sci. U. S. A.* **102**, 5126–5131 (2005).

61. J. C. Nussbaum, S. J. Van Dyken, J. von Moltke, L. E. Cheng, A. Mohapatra, A. B. Molofsky, E. E. Thornton, M. F. Krummel, A. Chawla, H.-E. Liang, R. M. Locksley, Type 2 innate lymphoid cells control eosinophil homeostasis. *Nature* **502**, 245–248 (2013).

62. A. Cortini, U. Ellinghaus, T. H. Malik, D. S. Cunninghame Graham, M. Botto, T. J. Vyse, B cell OX40L supports T follicular helper cell development and contributes to SLE pathogenesis. *Ann. Rheum. Dis.* **76**, 2095–2103 (2017).

63. R. I. Nurieva, X. M. Mai, K. Forbush, M. J. Bevan, C. Dong, B7h is required for T cell activation, differentiation, and effector function. *Proc. Natl. Acad. Sci. U. S. A.* **100**, 14163–14168 (2003).

64. S. Z. Josefowicz, R. E. Niec, H. Y. Kim, P. Treuting, T. Chinen, Y. Zheng, D. T. Umetsu, A. Y. Rudensky, Extrathymically generated regulatory T cells control mucosal TH2 inflammation. *Nature* **482**, 395–399 (2012).

65. A. Burich, R. Hershberg, K. Waggie, W. Zeng, T. Brabb, G. Westrich, J. L. Viney, L. Maggio-Price, Helicobacter-induced inflammatory bowel disease in IL-10- and T cell-deficient mice. *Am. J. Physiol. Gastrointest. Liver Physiol.* **281**, G764-78 (2001).

66. A. P. Heinen, F. Wanke, S. Moos, S. Attig, H. Luche, P. P. Pal, N. Budisa, H. J. Fehling, A. Waisman, F. C. Kurschus, Improved method to retain cytosolic reporter protein fluorescence while staining for nuclear proteins. *Cytometry A* **85**, 621–627 (2014).

67. L. W. Collison, D. A. A. Vignali, In vitro Treg suppression assays. *Methods Mol. Biol.* **707**, 21–37 (2011).

68. W. Hu, Z.-M. Wang, Y. Feng, M. Schizas, B. E. Hoyos, J. van der Veeken, J. G. Verter, R. Bou-Puerto, A. Y. Rudensky, Regulatory T cells function in established systemic inflammation and reverse fatal autoimmunity. *Nat. Immunol.* **22**, 1163–1174 (2021).

69. M. Feuerer, L. Herrero, D. Cipolletta, A. Naaz, J. Wong, A. Nayer, J. Lee, A. B. Goldfine, C. Benoist, S. Shoelson, D. Mathis, Lean, but not obese, fat is enriched for a unique population of regulatory T cells that affect metabolic parameters. *Nat. Med.* **15**, 930–939 (2009).

15   **Author contributions:**

Conceptualization: JS, TYH

Methodology: JS, TY, JMV, CG, MJS, TYH

Resources: HR, TV, ANJM, MSC, MH, DRW, HJF, RR, AL, TYH

Investigation: JS, TY, JMV, OB, YS, SR, CG, WL, HW, SKW, SP, CS, SM, AS, JB, PP, KY, TYH

20   Visualisation: JS, TY, JMV, TYH

Funding acquisition: JS, TYH

Project administration: JS, TYH

Supervision: TYH

Writing – original draft: JS, TYH

25   Writing – review & editing: JS, TY, JMV, ANJM, MSC, HJF, MH, DRW, RR, AL, TYH

Competing interests:

The authors have no competing interests.

30   **Data and materials availability**:

Sequencing data have been deposited under the accession number GSE230599.

Figures and Figure Legends
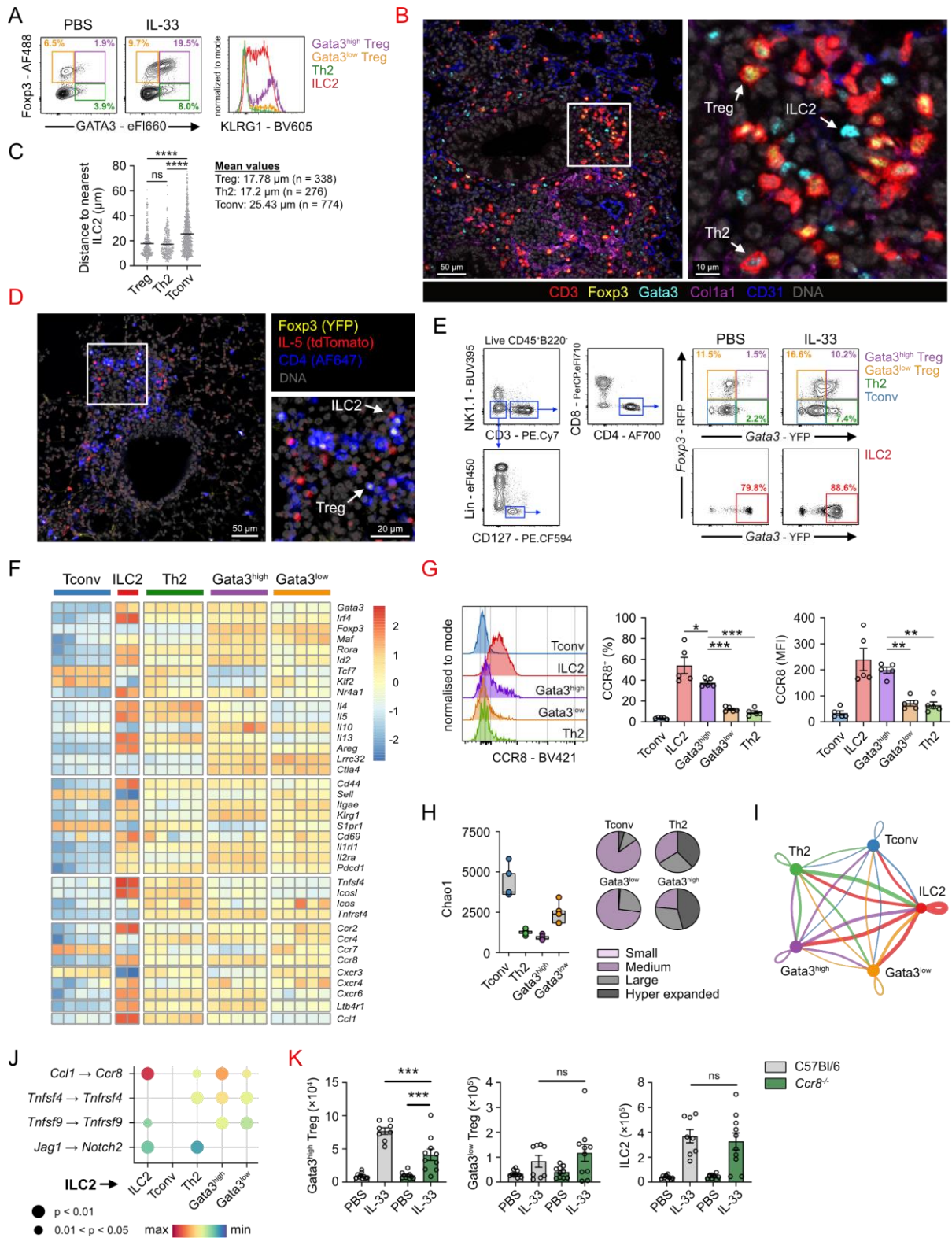
Fig. 1. Type-2 effector and regulatory lymphocytes express gene-signatures that enforce localisation and enable crosstalk mechanism in the inflamed lung niche.

A-C. Wild-type (C57Bl/6) mice were treated with PBS or IL-33 (200 ng, i/n) on day 0 and 1 followed by analysis of the lungs on day 5 for the indicated CD4+ T cell subsets (pre-gated on CD3+CD4+CD8-

NK1.1$^-$B220$^-$CD45$^+$ live cells) (*left*) and expression of KLRG1 on the indicated cell-types (*right*) (**A**). Multiplex IF microscopy of IL-33-treated lung sections allowed the identification of CD3$^+$Foxp3$^-$Gata3$^-$ Tconv, CD3$^+$Foxp3$^-$Gata3$^+$ Th2, CD3$^+$Foxp3$^+$ Treg and CD3$^-$Foxp3$^-$Gata3$^+$ ILC2 (**B**), followed by automated analysis of distances between the indicated cell-types (**C**, *see Fig. S1E*).

5 **D.** ILC2 (*Il5^{tdTom+}*CD4$^-$) and Tregs (*Foxp3^{YFP+}*CD4$^+$) were visualised in precision cut lung sections of IL-33-treated *Il5$^{tdTom/+}$Foxp3^{YFP}* mice.

E-K. *Gata3^{YFP}Foxp3^{RFP}* mice were treated with PBS or IL-33 (200 ng, i/n) on day 0 and 1, followed by analysis of the lungs on day 5 to identify CD4$^+$ T cell-subsets and ILC2 (**E**). Bulk RNA-seq data of the indicated populations (top row), flow-sorted from the lungs of *Gata3^{YFP}Foxp3^{RFP}* reporter mice (**F**), and

10 analysis of percent-expression (*middle*) and mean fluorescence intensity *(right)* of CCR8 on the indicated populations (**G**). TCR diversity analysis was performed on the transcriptomic data of the indicated T cell populations (left); pie charts show proportions of the indicated clonal subgroups (right) in the indicated T cell populations (**H**). CellChat analysis was performed on the indicated populations to predict homotypic and heterotypic interactions; colour of the lines represent direction (i.e. ligand

15 expression by same colour cell), while width represents the number of interactions (**I**). Several interactions whereby ILC2 were predicted to engage themselves, or the indicated T cell population (bottom axis). (**J**). Wild-type or *Ccr8$^{-/-}$* mice were treated with PBS or IL-33 on days 0 and 1, followed by quantification of the indicated populations in the airways on day 5 (**K**).

20 Microscopy images are representative of 2(**B**) or 3(**D**) independent experiments. Heat map shows expression represented as z-score (**F**). Histogram images are representative of >3(**A**) or 2(**G**) independent experiments. Bar graphs indicate mean (±SEM) and show representative data 2(**C**), 3(n=5,5,5,5,5; **G**), and 2(n=6,4,6,6; **K**) independent experiments. ns = not significant, **** = p ≤ 0.0001.
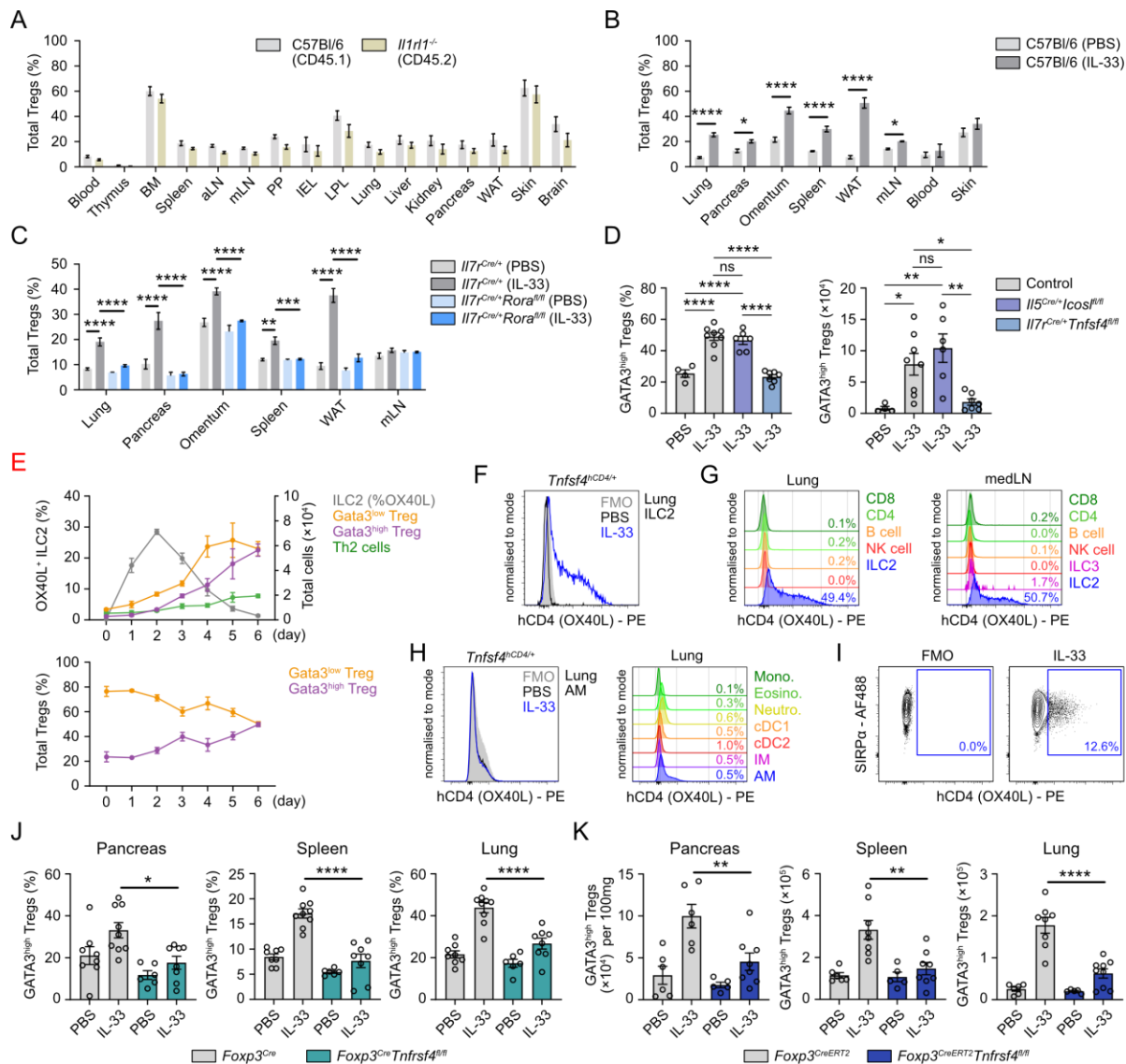
Fig. 2. ILC2 and the OX40L-OX40 signalling axis control tissue-specific Gata3^{high} Treg responses to IL-33.

Donor derived wild-type (C57Bl/6) and *Il1rl1^{-/-}* tissue-resident Tregs were quantified in the indicated tissues of untreated (50:50, WT/KO) bone marrow chimeric mice (**A**). Tregs were quantified in the indicated tissues of PBS or IL-33-treated (500 ng i/p on day 0 and 1, tissue collection on day 5) wild-type mice (**B**), and *Il7r[Cre/+]* or *Il7r[Cre/+]Rora^{fl/fl}* mice (**C**). Lung Gata3^{high} Tregs (% of Tregs, left; total numbers, right) were quantified in PBS or IL-33 treated (200 ng i/n on day 0 and 1, tissue collection on day 5) mice of the indicated genotypes (**D**). Wild-type mice were intranasally dosed with IL-33 on days 0 and 1, followed by the analysis of lungs at the indicated time points to determine OX40L expression by ILC2 (top, left axis) or the total numbers of the indicated cell types (top, right axis) (**E**); the percentage of Gata3^{high} and Gata3^{low} Tregs was measured in the lungs at different time points (bottom). **F-I.** *Tnfsf4[hCD4/+]* mice were treated with IL-33 or PBS (200ng i/n on day 0 and 1, tissue collection on day 3) followed by measurement of hCD4 on lung ILC2 (**F**) and the indicated lymphocytes in the lung

24

and mediastinal lymph node (**G**), the indicated lung myeloid cells (**H**, representative staining on alveolar macrophages shown left), and cDC2 in the medLN (**I**).

J-K. Mice of the indicated genotypes were treated with PBS or IL-33 (500ng i/p) on day 0 and 1, followed by quantification of Gata3^{high} Treg percentages (as a % of Tregs) (**J**) and numbers (**K**) in the indicated organs on day 5 (all mice were treated with tamoxifen in **K**).

Dot plots show representative gating strategy; numbers indicate percent of gated cells. Fluorescence minus one (FMO), Bone marrow (BM), axillary (a)LN, mesenteric (m)LN, Peyer's patch (PP), intraepithelial lymphocytes (IEL), lamina propria lymphocytes (LPL), white adipose tissue (WAT). Bar graphs indicate mean (±SEM) and show data of one experiment (n=4 for all; **A**), representative data of 2 independent experiments (n=5,5,4,5,5,5,5,5,5,5,5,5,5,5,5,5; **B**), or pooled data from 2 independent experiments (n=8,9,7,9,6,8,7,9,7,7,5,6,6,8,7,9,4,4,4,4,4,4,4,4; **C**), (n=4,8,6,7; **D**), (n=4 for day 0, 6 for all other days; **E**), (n=8,9,6,8, left; n=8,9,6,8, middle; n=8,9,6,8, right; **J**), (n= 6,6,5,8, left; n=6,8,5,8, middle; n=6,8,5,9, right; **K**) mice per group. ns = not significant, * = p ≤ 0.05, ** = p ≤ 0.01, *** = p ≤ 0.001, **** = p ≤ 0.0001.
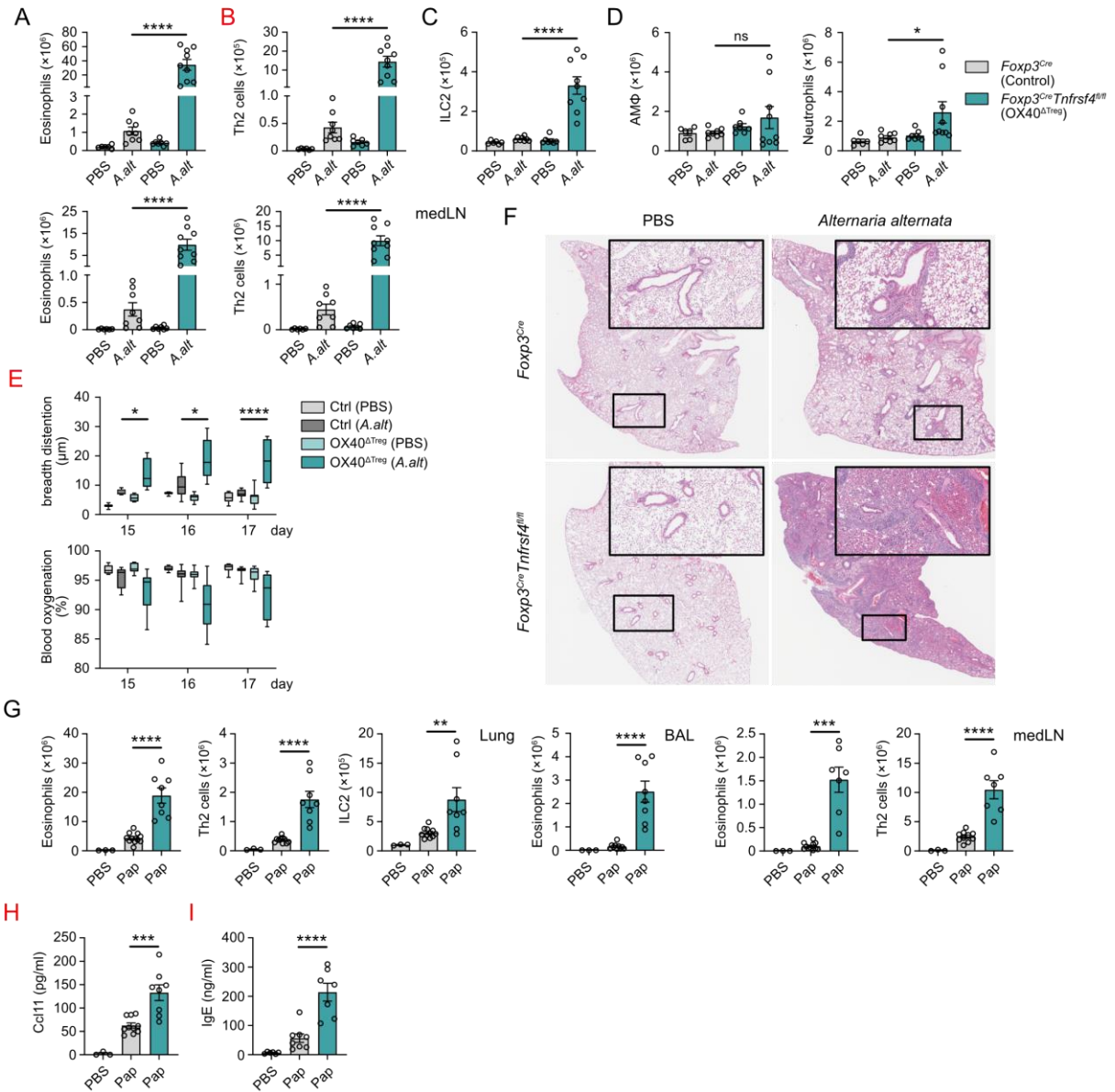
Fig. 3. Treg-intrinsic OX40 is critical for the effective control of type-2 inflammation.

A-F. Mice of the indicated genotypes were treated intranasally with *Alternaria alternata* or PBS on days 0, 1 and 14, followed by sacrifice on day 20. Flow cytometric quantification of lung (top) and medLN (bottom) eosinophil (**A**) and Th2 cell numbers (**B**). Flow cytometric quantification of ILC2 (**C**) and alveolar macrophage (left) and neutrophil (right) cell numbers (**D**). Mice were analysed by pulse oximetry for breadth distention (top) and blood oxygenation (bottom) on the indicated days (**E**). Representative H&E staining of lung sections (**F**).

G-I. Mice were treated intranasally with papain or PBS on days 0, 1 and 14, followed by sacrifice on day 20. Flow cytometric quantification of lung eosinophil, Th2 and ILC2 cell numbers (left), BAL eosinophil cell numbers (middle), and medLN eosinophil and Th2 cell numbers (right) (G). BAL concentration of Ccl11 (**H**). Serum concentration of IgE (**I**).

26

Representative histology images shown of 2 independent experiments. Bar graphs indicate mean (±SEM) and show combined data of 2 independent experiments with (n=6,8,7,9; **A-E**) and (n=3,10,8; **G, H**) or (n=6, 8, 7; **I**) mice per group. * = p ≤ 0.05, ** = p ≤ 0.01, *** = p ≤ 0.001, **** = p ≤ 0.0001.
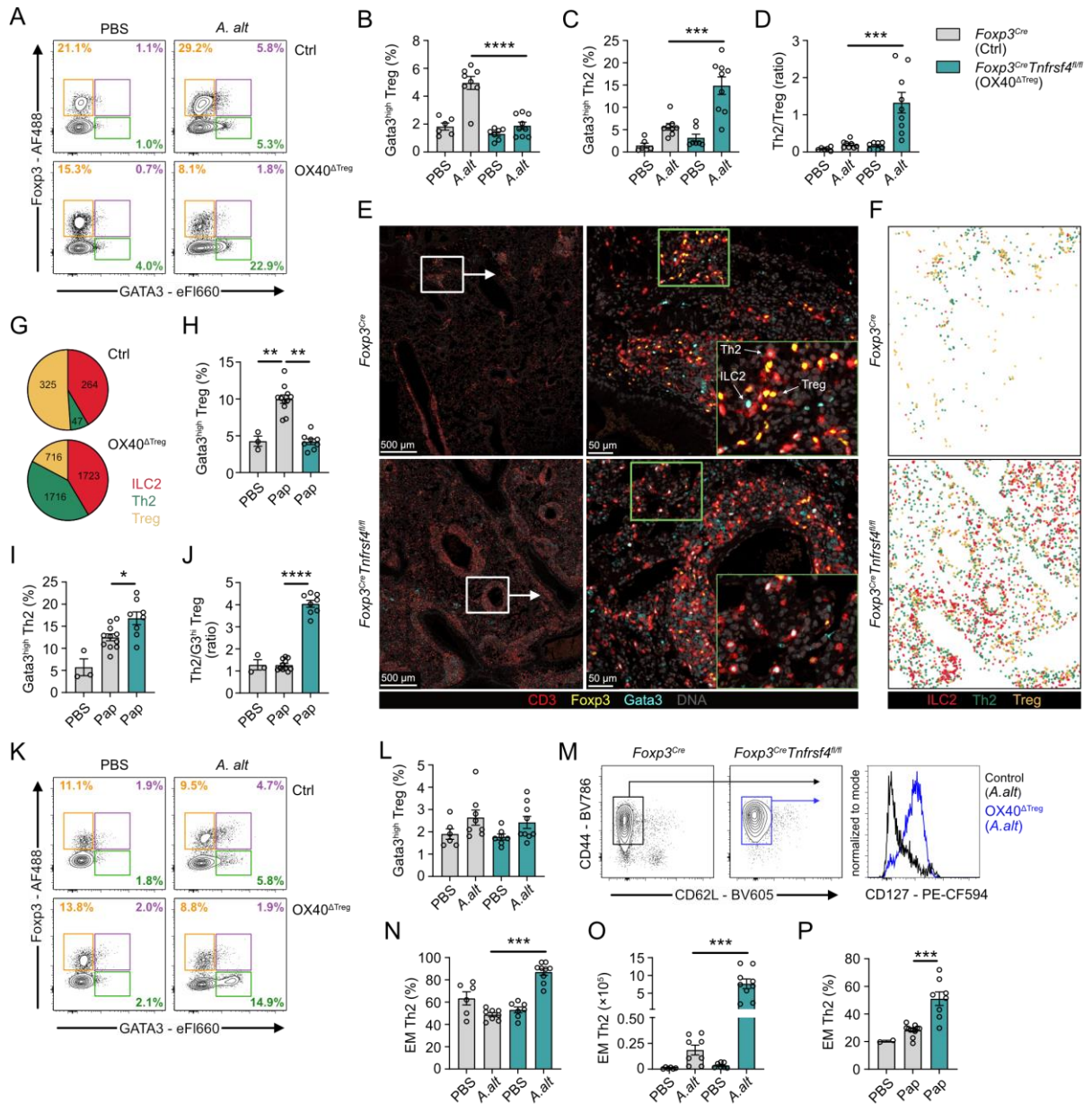
Fig. 4. Allergen exposed OX40^ΔTreg mice have impaired Gata3^high Treg induction and amplified effector memory Th2 cell expansion.

A-G. The lungs of PBS- or *Alternaria alternata*-treated mice of the indicated genotypes were analysed for percentages of (Live CD45$^+$CD3$^+$CD4$^+$CD44$^+$CD62L$^-$ pre-gated) Gata3^{low} and Gata3^{high} Tregs (yellow and purple), or Th2 cells (green) by flow cytometry (representative dot plots in **A**, treated i/n on day 0, 1 and 14, sacrificed on day 20), followed by quantification of the percentage of Gata3^{high} Tregs (**B**) and Th2 cells (**C**) or indicated cell ratios (**D**). Multiplex IF microscopy of lung sections allowed the identification of CD3$^+$Foxp3$^-$Gata3$^+$ Th2, CD3$^+$Foxp3$^+$ Treg and CD3$^-$Foxp3$^-$Gata3$^+$ ILC2 (**E**), followed by automated analysis of cell-type densities using HALO (**F, G**).

H-J. The percentage of Gata3^{high} Tregs (% of total CD4$^+$) (**H**) and Th2 cells (% of total CD4$^+$) (**I**) or indicated cell ratios (**J**) were measured in the lungs of *Foxp3^Cre* or *Foxp3^Cre Tnfrsf4^fl/fl* mice treated with PBS or papain (same dosing as in A).

28

K-P. The medLN of PBS, *Alternaria alternata* or papain treated mice of the indicated genotypes were analysed for percentages of Gata3^{low} and Gata3^{high} Tregs (yellow and purple), or Th2 cells (green) by flow cytometry (**K**). The percentages of Gata3^{high} Tregs (% of total CD4$^+$) were measured (**L**). Th2 cells were further analysed for expression of CD127 on CD44$^+$CD62L$^-$ cells (**M**), followed by measurement of CD44$^+$CD62L$^-$CD127$^+$ effector memory (EM) Th2 cell percentages (% of CD44$^+$CD62L$^-$ Th2) (**N**) and numbers (**O**). Similarly, EM Th2 cell percentages (% of CD44$^+$CD62L$^-$ Th2) were measured in PBS and papain-treated mice (**P**).

Dot plots show representative gating strategy; numbers indicate percent of gated cells. Bar graphs indicate mean (±SEM) and show combined data of 2 independent experiments with (n=6,8,7,9; **B-D**, **L**, **N**, **O**) and (n=3,10,8; **H-J**, **P**) mice per group. * = p ≤ 0.05, ** = p ≤ 0.01, *** = p ≤ 0.001, **** = p ≤ 0.0001.
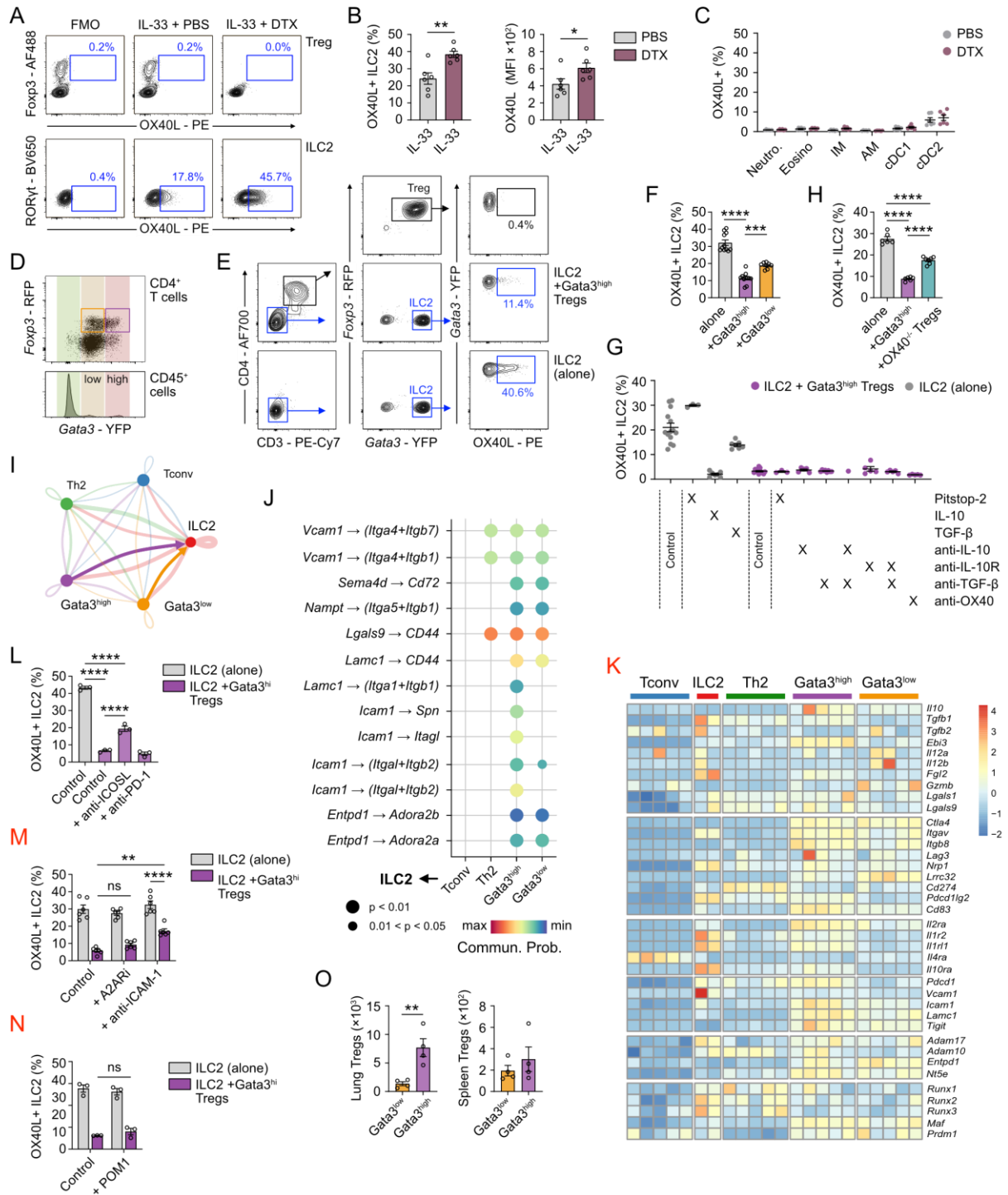
Fig. 5. Gata3^{high} Tregs directly control OX40L availability on ILC2 and preferentially home to the inflamed lung.

A-C. *Foxp3^{DTR}* mice were treated intranasally with IL-33 plus *diphtheria* toxin (DTX) or PBS on days 0, and 1, and sacrificed on day 3. Representative flow cytometric identification of OX40L$^+$ lung Treg and ILC2 cells (**A**), and quantification of OX40L$^+$ ILC2 cells expressed as percentage (left) and mean fluorescence intensity (right) (**B**), and percent OX40L$^+$ myeloid cells (**C**).

D-H. Gata3^high (purple) or Gata3^low (orange) Tregs were identified, and flow sorted alongside ILC2 from *Gata3^{YFP}Foxp3^{RFP}* mouse lungs (**D**, *see also Fig. S1G*); ILC2 were co-cultured alone or with the indicated Treg populations for 20 hours followed by measurement of OX40L expression on ILC2 or Tregs by flow cytometry (**E** shows representative gating, **F** show percent OX40L⁺ ILC2 for each condition). ILC2 monocultures (grey) or Gata3^high Treg co-cultures (purple) were supplemented with the indicated reagents, followed by measurement of OX40L expression on ILC2 (**G**). OX40-deficient Tregs were flow-sorted from *Foxp3^{Cre}Tnfrsf4^{fl/fl}* mice and compared with Gata3^high Tregs in their ability to suppress OX40L on ILC2 (**H**).

I-N. Computational analysis using CellChat of Treg-to-ILC2 interactions (**I**) revealed several pathways that were selectively enriched or present in Gata3^high Tregs (**J**). Transcriptome of selected genes involved in immunosuppression in the indicated populations (**K**). ILC2 monocultures (grey) or Gata3^high Treg co-cultures (purple) were supplemented with the indicated reagents, followed by measurement of OX40L expression on ILC2 (**L-N**).

O. Gata3^high or Gata3^low Tregs were flow-sorted from IL-33-treated *Gata3^{YFP}Foxp3^{RFP}* mouse lungs followed by adoptive transfer of 2.5×10^4 cells into *Rag2^{-/-}* recipient mice. Two days later the lungs and spleens of recipient mice were analysed for numbers of Foxp3^{RFP+} Tregs (**O**).

Dot plots show representative gating strategy; numbers indicate percent of gated cells. Heat map shows expression represented as z-score (**K**). Bar graphs indicate mean (±SEM) and show representative (n=3,3,3,3; **L**) or combined (n=6,6; **B**, **C**) data of 2 independent experiments, or combined data from 1-3 independent experiments (n=14,3,7,7,3,5,8,1,5,5,5; **H**), or combined data of >3 independent experiments (n=11,11,8; **F**), (n=6,6,7; **G**), (n= ;**M**) (n= ;**N**) (n=4,4; **O**) experiments (mice or individual co-cultures per group). * = p ≤ 0.05, ** = p ≤ 0.01, *** = p ≤ 0.001, **** = p ≤ 0.0001.
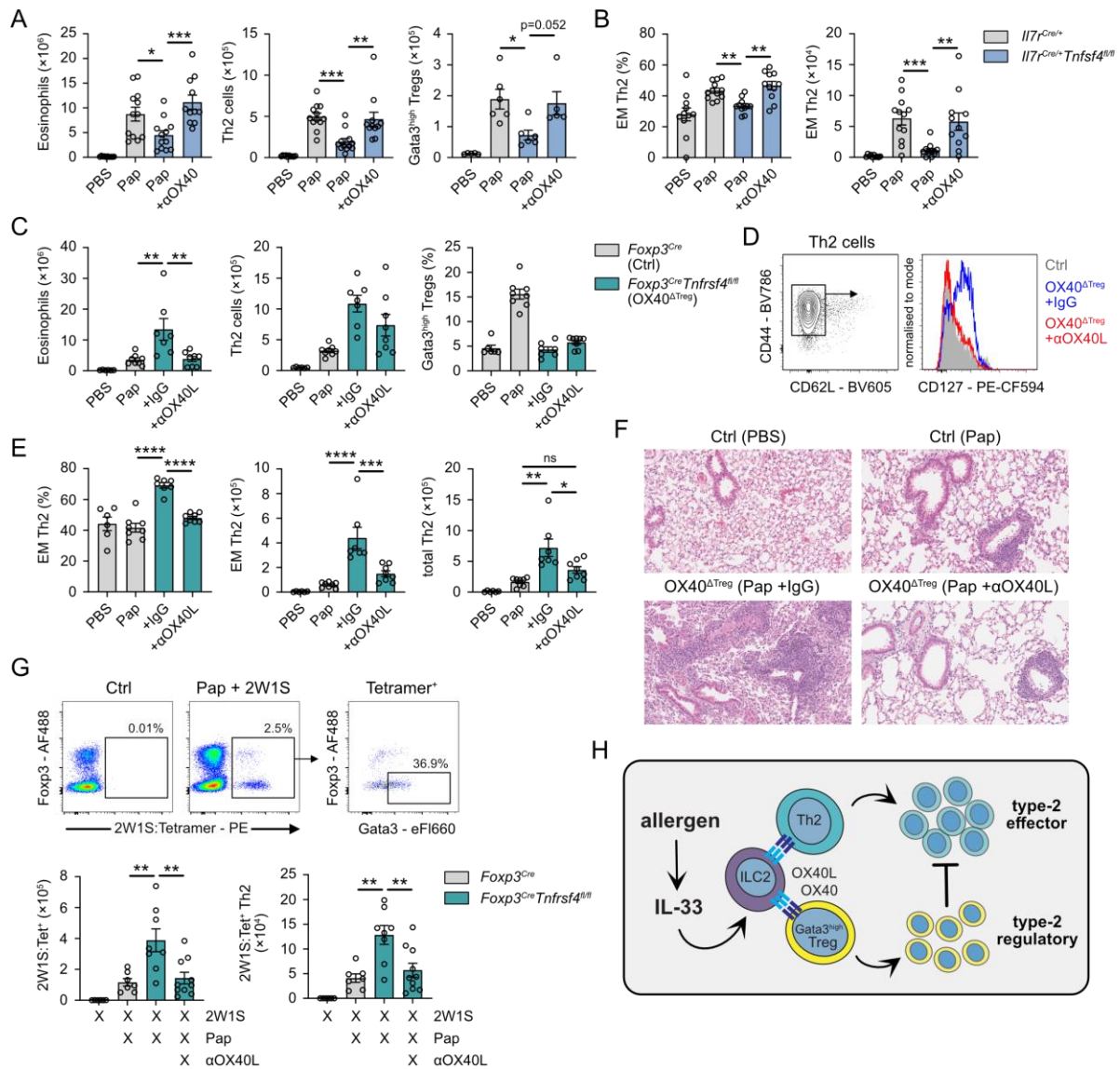
Fig. 6. OX40⁺ Tregs control adaptive type-2 immunity by modulating OX40L availability.

A-B. Mice of the indicated genotypes were treated intranasally with PBS or papain on days 0, 1 and 14, plus OX40 agonist (mouse IgG1) as indicated (*see Fig. S8B*) followed by sacrifice on day 20. Flow cytometric quantification of lung eosinophil, Th2 cell number and Gata3^{high} Treg percentage (**A**). medLN effector memory Th2 percentage (% of CD44⁺CD62L⁻ Th2) (left) and numbers (right) were measured (**B**).

C-F. Mice of the indicated genotypes were treated intranasally with PBS or papain on days 0, 1 and 14, plus anti-OX40L or rat IgG isotype control as indicated (*see Fig. S8C*) followed by sacrifice on day 20. Flow cytometric quantification of lung eosinophil, total Th2 cell and Gata3^{high} Treg cell numbers (**C**). Representative flow cytometric identification (**D**) and quantification (**E**) of total medLN EM Th2 (left and middle, as % of CD44⁺CD62L⁻ Th2 or cell numbers) or total Th2 (right) cell numbers. Representative H&E staining of lung sections (**F**).

G. Mice were treated intranasally with PBS (+2W1S peptide) or papain (+2W1S peptide) on days 0, 1 and 14, plus anti-OX40L as indicated (*see Fig. S8C*) followed by sacrifice on day 20. 2W1S:tetramer-

positive CD4$^+$ cells were detected by flow cytometry (PBS + 2W1S and papain + 2W1S treated *Foxp3^{Cre}* control mice shown, left), followed by intracellular detection of Foxp3 and Gata3 (right) (**G**, top) 2W1S:tetramer$^+$ total (left) and Th2 (right) cells were quantified in the lungs of mice treated as indicated (**G**, bottom).

H. Graphical abstract.

Representative histology images shown of 2 independent experiments. Dot plots show representative gating strategy; numbers indicate percent of gated cells. Bar graphs indicate mean (±SEM) and show combined or representative data of two independent experiments with (n=11,12,12,11; **A-B**, n=5,6,6,5; right panel of **A**), (n=6,8,7,8; **C**, **E**) and (n=6,7,8,10; **G**) mice per group. ns = not significant, * = p ≤ 0.05, ** = p ≤ 0.01, *** = p ≤ 0.001, **** = p ≤ 0.0001.

(SUPPLEMENTARY MATERIAL)

The magnitude of adaptive type-2 immunity is locally constrained via a Gata3$^{\text{high}}$ Treg – ILC2 axis

Materials and Methods

Supplemental Figure 1
Supplemental Figure 2
Supplemental Figure 3
Supplemental Figure 4
Supplemental Figure 5
Supplemental Figure 6
Supplemental Figure 7
Supplemental Figure 8

Supplemental Table 1
Supplemental Table 2

Materials and Methods

Mice

Foxp3^{DTR} (*1*) (JAX #016958), *Foxp3$^{YFP-Cre}$* (*2*) (JAX #016959), *Foxp3^{CreERT2}* (*3*) (JAX #016961), *Foxp3^{RFP}* (*4*) (JAX #008374), *Il5$^{tdTom-Cre}$* (*5*) (JAX #030926) were bought from JAX, and were maintained in the Cancer Research UK – Cambridge Institute (CRUK-CI) animal facility, under specific-pathogen-free conditions along with *Il7r$^{Cre/+}$* (provided by Prof. Rodewald), *Il7r$^{Cre/+}$Rora$^{fl/fl}$*, *Il7r$^{Cre/+}$Tnfsf4$^{fl/fl}$* (*Tnfsf4$^{fl/fl}$* mice (*6*) provided by Prof. Vyse and Prof. Botto), *Tnfrsf4$^{fl/fl}$*, *Foxp3$^{YFP-Cre}$Tnfrsf4$^{fl/fl}$*, *Foxp3^{CreERT2}Tnfrsf4$^{fl/fl}$*, *Gata3$^{YFP/YFP}$* (*7*) (provided by Prof. Fehling), *Gata3$^{YFP/YFP}$Foxp3^{RFP}*, *Il13^{tdTom}* (provided by Prof. McKenzie), *Il13^{tdTom}Foxp3$^{YFP-Cre}$*, *Il5$^{tdTom-Cre}$Foxp3$^{YFP-Cre}$* mice, *Il5$^{tdTom-Cre}$Icosl$^{fl/fl}$* (*8*) and *Tnfsf4^{hCD4}* all in the CD57BL/6 background. Wild-type C57BL/6J mice were purchased from Charles River. Animal work was conducted under project licenses PD7484FB9 or PF993249 at the CRUK-CI (with approval from the Cancer Research UK - Cambridge Institute, Animal Welfare Ethical Review Body) all in accordance with Home Office regulation. CD45.1 mice and *Il1rl1$^{-/-}$* mice were maintained in the Medical Research Councils ARES facility (Babraham, UK). *Ccr8$^{-/-}$* mice were maintained in the Cambridge University Biomedical Services Gurdon Institute animal facility. Experiments involving these strains (all on the C57BL/6 background) were performed in these facilities. Mice were sex and age matched whenever possible, and most mice were used at 8-12 weeks of age.

Tnfrsf4$^{fl/fl}$ mouse generation

The *Tnfrsf4$^{tm1a(EUCOMM)Wtsi}$* ES cells were purchased from the European Mouse Mutant Cell Repository (EuMMCR, HelmholtzZentrum Munchen, GB) and injected into wild type CD1 8-cell stage embryos. Microinjected embryos were cultured in KSOM +AA media (KCl, enriched simplex optimisation medium with amino acid supplement, Zenith Biotech) at 37°C with 95% humidity and 5% CO_2 until they reached the blastocyst stage. Blastocysts were transferred into pseudopregnant recipients. The resulting F0 mice were bred to C57BL/6 mice, proving germline transmission. Superovulated *Tnfrsf4$^{(fl/+)}$* female mice were further *in vitro* fertilised by C57BL/6 flp sperm to remove the neo-cassette.

Tnfsf4^{hCD4} mouse generation

Stock animals (also known as C57BL/6J-Ox40l^{em1H}/H) were generated by the Mary Lyon Centre at MRC Harwell (MLC) via pronuclear injection of CRISPR/Cas9 reagents into 1-cell stage embryos. The MLC generated this mouse strain as part of its commitment to the Genome Editing Mice for Medicine project funded [MC_UP_1502/3] by the Medical Research Council. The research reported in this publication is solely the responsibility of the authors and does not necessarily represent the official views of the Medical Research Council.

In vivo procedures

rmIL-33 (0.5 µg, Biolegend), diphtheria toxin (10 ng/g, Sigma), 2W1S peptide (25 µg, Genescript) and anti-OX40L mAb (200 µg, Clone RM134L, BioXcell) were administered by intraperitoneal injection in 200 µl of PBS. Anti-OX40L mAb was treated beforehand with 0.05 units of PNGaseF (Promega V483A) per µg of antibody. Samples were incubated at 37°C overnight and purification of the antibody from the enzyme was achieved through size-exclusion dialysis (Pur-A-Lyzer Maxi Dialysis Kit, Maxi 50000, Sigma-Aldrich). Successful de-glycosylation was confirmed by SDS-PAGE electrophoresis. For intranasal administration, mice were anesthetized by isoflurane inhalation, and received rmIL-33 (0.2 µg, Biolegend), Papain (10-15 µg, Sigma), *A. alternata* (10 µg, Greer Laboratories), house dust mite (100 µg, Greer Laboratories), ragweed pollen extract (300 µg, Greer Laboratories), or anti-OX40 mAb (40 µg, OX86 mIgG1, Antibody and Vaccine group, University of Southampton) in 40 µl of PBS. For induction of Cre-ERT2–mediated recombination, mice were fed tamoxifen-containing food (TD.55125; Envigo). Labelling of circulating leukocytes to evaluate tissue-residency was achieved by i.v. injection of 3 µg anti-CD45.2-PE (clone 104, Biolegend) antibody 3 min prior to sacrifice.

Mixed bone marrow transplantation

CD45.1 x CD45.2 recipient mice were lethally irradiated (2 doses of 5.5 Gy) followed by intravenous transplantation of 2×10^6 bone marrow cells, as a 50/50 mix of CD45.1 and ST2-KO. Mice were given Baytril in drinking water for 3 weeks and used for analysis at 8 weeks post-transplant. 2 µg of anti-CD45-biotin was injected i.v. 3 min prior to sacrifice to label circulating leukocytes.

Pulse oximetry

The right hind legs of mice were shaved using an electric razor and then depilated using hair removal cream before pulse oximetry (MouseOX Plus Pulse Oximeter, STARR Life Sciences Corp., PA, USA). Mice were anaesthetized (3% isoflurane for induction, followed by 1.5% for maintenance, v/v in supplied air) and kept on a warming pad throughout the measurement. Blood oxygenation and breadth distention were recorded using the ThighClip mouse thigh sensor and analysed using MouseOX Plus v1.5 software (STARR Life Sciences Corp., PA, USA).

Histology

Tissues were fixed in 10% neutral buffered formalin and embedded in paraffin before sectioning into 3-µm slices. Sample embedding, sectioning, and histological stainings (Hematoxylin and Eosin, Periodic Acid Schiff, Masson's Trichrome) were conducted by the CRUK-CI Histology Core. Scoring of the colon and lung sections was done by a board-certified veterinary pathologist blinded to the groups and experimental conditions, as previously described. (*9*, *10*)

Single cell preparation

Lung

Cell suspensions were prepared by mechanical dissociation, followed by digest in 4 ml of RPMI-1640 containing collagenase I (563 U/ml) and DNase I (0.225 mg/ml) for 1 hour at 37°C on a shaker (220 rpm), followed by filtration through a 70 μm strainer and red blood cell (RBC) lysis.

Pancreas

Pancreata were weighed, then mechanically dissociated, followed by digest in 5 ml of HBSS containing collagenase I (375 U/ml), DNase I (0.15 mg/ml) and Soybean Trypsin inhibitor (Sigma, 0.05 mg/ml) for 30 minutes at 37°C on a shaker (220 rpm), followed by dissociation on a syringe and needle, filtration through a 70 μm strainer and RBC lysis.

Omentum and Adipose tissue

Tissues were weighed, then digested in 0.5 ml of HBSS containing collagenase I (375 U/ml), DNase I (0.15 mg/ml) and Soybean Trypsin inhibitor (Sigma, 0.05 mg/ml) for 45 minutes at 37°C on a shaker (1100 rpm), followed by filtration through a 70 μm strainer. Strainers were further washed with 10 ml warm RPMI-10%FCS.

Spleen

Spleens were strained through a 70 μm filter in RPMI-1640 before RBC lysis.

Mediastinal lymph node

Cell suspensions were prepared by mechanical dissociation, followed by digest in 0.5 ml of RPMI-1640 containing collagenase I (375 U/ml) and DNase I (0.15 mg/ml) for 45 min at 37°C on a shaker (1100 rpm), followed by red blood cell (RBC) lysis.

BAL

BAL cells and fluid were obtained in 1 ml PBS.

Flow cytometry

Single cells were incubated with anti-mouse CD16/32 (Thermo Fisher) to block Fc receptors. For intracellular staining we used the Foxp3/Transcription Factor Kit (Thermo Fisher), except when co-staining YFP and Foxp3, where the protocol described by Heinen *et al.* was followed (*11*). For intracellular cytokine detection, single cells were stimulated with 1× protein transport inhibitor, 1× cytokine stimulation cocktail (Thermo Fisher Scientific) in culture medium (RPMI 1640, 10% FCS) at 37 °C for 3 h before staining. Data was acquired on a BD Fortessa or Symphony instrument. Cells were quantified using CountBright beads. Data was analysed using FlowJo X (Tree Star).

The following antibodies were used in this study, with clones, venders, and fluorochrome as indicated:

CD8 (53-6.7, eBioscience, PerCP-eFluor710), CD45 (30-F11, Biolegend, BV510), NK1.1 (PK136, BD, BUV395), CD4 (RM4-5, eBioscience, AF700), human CD4 (RPA-T4, Biolegend, PE), B220 (A3-6B2, eBioscience, APC-eFluor780), CD127 (SB/199, BD, PE-CF594), CD44 (IM7, Biolegend, BV785), CD62L (MEL-14, Biolegend, BV605), OX40L (RM134L, Biolegend, AF647 or eBioscience, PE), OX40 (OX-86, eBioscience, PE), Ccr8 (SA214G2, Biolegend, BV421), ICOSL (HK5.3, Biolegend, PE), KLRG1 (2F1, Biolegend, BV605 or eBioscience, PerCP-eFluor710), ST2 (RMST2-2, eBioscience, PE), TCRβ (H57-597, Biolegend, PE), Gata3 (TWAJ, eBioscience, eFluor660), Foxp3 (FJK-16s, eBioscience, AF488 or eFluor660), RorgT (Q31.378, BD, BV650), IL-5 (TRFK5, BD Biosciences, APC), FceRIa (MAR-1, eBioscience, PerCP-eFluor710), CD172α (P84, Biolegend, AF488), Siglec-F (1RNM44N, eBioscience, SB600), XCR1 (ZET, Biolegend, BV650), CD64 (X54-5/7.1, Biolegend, BV711), CD11b (M1/70, Biolegend, BV785), I-A/I-E (CI2G9, BD, BUV395), CD11c (N418, eBioscience, AF700), F4/80 (BM8, eBioscience, APC-eFluor780), Ly6G (1A8-Ly6g, eBioscience, PE-eFluor610), Ly-6C (HK1.4, eBioscience, PE-Cy7). Lineage cocktail contained either CD5 (53-7.3), CD19 (1D3), CD11b (M1/70), CD11c (N418), FcεR1α (MAR-1), F4/80 (BM8), Ly-6C/G (Rb6-8C5), and Ter119 (TER-119), or CD3 (145-2C11), NK1.1 (PK136), CD5 (53-7.3), CD19 (1D3) and B220 (RA3-6B2), all on eFluor450 (eBioscience). Dead cells were excluded with the fixable viability dye UV455 or eFluor780 (eBioscience).

ILC2 and Treg cell isolation and co-culture

Single cell suspensions from IL-33-sensitised lungs from $Gata3^{YFP/YFP}Foxp3^{RFP}$ mice were used to isolate ILC2s (Live CD45$^+$CD3$^-$CD4$^-$Foxp3$^{(RFP)-}$Gata3$^{(YFP)high}$) and Gata^{high} and Gata^{low} Treg cells (Live CD45$^+$CD3$^+$CD4$^+$Foxp3$^{(RFP)+}$Gata3$^{(YFP)high\ or\ low}$) by flow cytometry using a BD Melody instrument. Purified cells were co-cultured overnight in equal concentrations in RPMI-1640 supplemented with 10% FCS, 100 U/ml penicillin (Gibco), and 100 µg/ml streptomycin (Gibco), along with rmIL-33 (10 ng/ml, Biolegend), rhIL-2 (25 ng/ml, Peprotech) and rhIL-7 (10 ng/ml, Peprotech), and where indicated with additional Pitstop-2 (10 µM, Sigma), ADAM10/17 inhibitor - GW 280264X (0.5 µM, Tocris), A2A receptor antagonist – ZM 241385 (3 µM, Biotechne), or POM-1 inhibitor (50 µM, Biotechne), rhIL-10 (20 ng/ml, Biolegend), rhTGF-β1 (4 ng/ml, Peprotech), anti-IL10 mAb (20 µg/ml, BioXCell, clone JES5-2A5), anti-IL10R mAb (20 µg/ml, Biolegend, clone 1B1.3a), anti-TGF- β1,2,3 mAb (20 µg/ml, BioXCell, clone 1D11.16.8), anti-OX40 mAb (20 µg/ml, Antibody and Vaccine group, University of Southampton, clone OX-86), anti-PD1 (5 µg/ml, BioXCell, clone RMP1-14), anti-ICOSL (10 µg/ml, Biolegend, clone HK5.3), anti-ICAM-1 (0.5 µg/ml, eBioscience, clone YN1/1.7.4). Cells were cultured at 37°C in a humidified, 5% CO$_2$ incubator for 18 hours, before analysis by flow cytometry, qPCR or detection of soluble OX40L in supernatants.

qPCR analysis for *Tnfsf4*

RNA was extracted with the RNeasy Plus kit (Qiagen), and converted into cDNA using the High-Capacity RNA-to-cDNA Kit (Thermo Scientific), followed by qPCR using the TAKYON Low Rox Probe Master mix dTTP Blue (Eurogentec) and primers/probe pre-designed assays for *Tnfsf4* (Mm.PT.58.6713411) (Integrated DNA Technologies). To avoid misinterpretation due to cell number difference in between ILC2 mono-culture and co-culture with Tregs, *Tnfsf4* Ct values were not normalised to a housekeeping gene, having verified beforehand the absence of *Tnfsf4* transcript in Treg mono-culture. Results are expressed as arbitrary units set to 100 for the expression of *Tnfsf4* in ILC2 mono-culture in each independent experiment.

ELISA

Supernatants from ILC2 monocultures or ILC2 plus Treg co-cultures were collected and assessed for soluble OX40L by sandwich ELISA (Thermo Fisher), following manufacturer instructions. Serum and BAL samples from *Foxp3$^{YFP-Cre}$* and *Foxp3$^{YFP-Cre}$Tnfrsf4$^{fl/fl}$* mice were collected and assessed for IgE (Thermo Fisher) and Ccl11 (R&D Systems) by sandwich ELISA, following manufacturer instructions.

***In vitro* T cell suppression assay**

Assay was carried out according to Collison et al.(*12*) Briefly, a twofold titration series of FACS-sorted spleen and LN Treg (CD45$^+$CD3$^+$CD4$^+$CD8$^-$TCRβ$^+$YFP$^+$) cells starting from 25,000 cells per well was set up in U-bottom 96-well plates. 25,000 FACS-sorted, CellTrace Violet (Invitrogen)-labelled spleen and LN Tconv (CD45$^+$CD3$^+$CD4$^+$CD8$^-$TCRβ$^+$YFP$^-$) cells were then added to each well, in addition to anti-CD3/CD28 coated beads (Gibco) at a final concentration of 6.25 x10^4 beads/ml. Alternatively, FACS-sorted lung Gata3^{high} and Gata3^{low} Tregs were co-cultured with 25,000 CellTrace Violet-labelled lung Tconv cells per well at the specified ratios, together with anti-CD3/CD28 coated beads. Cells were incubated in a final volume of 200 μl IMDM with 10% FBS, 100 U/ml penicillin (Gibco), 100 μg/ml streptomycin (Gibco), 1x Glutamax (Gibco) and 5.5 μM β-mercaptoethanol (Gibco), and incubated in 5% CO2 at 37 °C for 4-5 days before analysis on a BD FACS Symphony. Results were expressed as described by Hu et al. (*13*).

Microscopy

For imaging of precision-cut lung slices (PCLS), *Il5$^{tdTom/+}$Foxp3$^{YFP-Cre}$* mice were injected with 200 ng rmIL-33 intranasally for 2 days. 5 days after the first injection, mice were sacrificed and lungs were inflated with 1 ml of 2% low melting point agarose diluted in PBS. 200 μm sections were prepared using a Leica VT 1200S Automated Vibrating Blade Microtome. PCLS were then washed in RPMI supplemented with 10% FCS for 15 min at 37°C. Lung slices were incubated in staining solution consisting of anti-CD4-AF647 (clone RM4-5, Invitrogen) and 10 μM Hoechst 33342 (Thermo Scientific) prepared in RPMI for 1 hour at 37°C prior to imaging. For imaging of whole pancreas explants, *Il13$^{tdTom/+}$Foxp3$^{YFP-Cre}$* mice were injected with 200 ng rmIL-33 intraperitoneally for 2 days and

sacrificed 3 days after the first injection. One day prior to sacrifice, mice were injected intraperitoneally with Hoechst 33342 (Thermo Scientific). PCLS and pancreas explants were imaged on an inverted laser-scanning confocal microscope (Stellaris 8, Leica Microsystems) with an attached pulsed Coherent Chameleon Ultra II laser, using a 25X 0.95NA water immersion objective lens. Hoechst and tdTomato were excited at 2-photon excitation wavelengths of 800 nm and 1040nm, respectively. YFP and AF647 were excited at single-photon excitation wavelengths of 488nm and 633nm, respectively.

Multiplex immunofluorescence imaging was performed on formalin-fixed paraffin-embedded lung sections using Opal multiplex IHC kits (Akoya Biosciences), following manufacturer instructions. Antigen retrieval was performed using 10mM sodium citrate (pH 6) and sections were stained using primary antibodies against Gata3 (abcam, ab199428), Collagen-I (abcam, ab34710), CD3 (abcam, ab11089), CD31 (Cell Signalling Technologies, 77699S), and Foxp3 (Thermo Scientific, 14-5773-82). After washing, sections were incubated with HRP-conjugated anti-rabbit (Akoya Biosciences) or anti-rat (abcam, ab214882) polymer-HRP secondary antibody for 15 minutes. The Opal Polaris 480, Opal 520, Opal 570, Opal 620, and Opal 690 reagents were used for visualisation of Gata3, Collagen-I, Foxp3, CD31, and CD3 respectively. Stained multiplex immunofluorescence sections were imaged on an inverted laser-scanning confocal microscope (Stellaris 8, Leica Microsystems) using a 25X 0.95NA water immersion objective lens. Large sections of tissue were imaged for downstream analysis as a maximum intensity projection (typically a z-stack of 10 µm, 40-60 tiles). Image analysis was performed using the HALO software (Indica Labs). Cell types were identified using the HighPlex-FL algorithm, and fine-tuned for cell types of interest detailed in the main text.

Bulk RNAseq

Treg (CD45$^+$CD3$^+$CD4$^+$CD8$^-$TCRβ$^+$YFP$^+$) and Tconv (CD45$^+$CD3$^+$CD4$^+$CD8$^-$TCRβ$^+$YFP$^-$) cells were sorted from spleens of $Foxp3^{YFP-Cre}Tnfrsf4^{fl/fl}$ mice using a BD Aria II cell sorter. Gata3^{high} and Gata3^{low} Treg cells (CD45$^+$Lin$^-$CD3$^+$CD8$^-$TCRβ$^+$CD4$^+$RFP$^+$YFP$^{hi/lo}$), Tconv and Th2 cells (CD45$^+$Lin$^-$CD3$^+$CD8$^-$TCRβ$^+$CD4$^+$RFP$^-$YFP$^{lo/hi}$) and ILC2s (CD45$^+$Lin$^-$CD3$^-$CD4$^-$YFP^{hi}) were sorted from lungs of IL-33-sensitised $Gata3^{YFP/YFP}Foxp3^{RFP}$ mice on a BD Symphony S6 sorter.

RNA was extracted using RNeasy plus micro kit (Qiagen) and 5 to 15 ng used as input material for library preparation. Libraries were generated with the NEBNext® Single Cell/Low Input RNA Library Prep Kit for Illumina (NEB) according to manufacturer's instructions. The pooled libraries were quantified with KAPA Library Quantification Kit for Illumina (Kapa Biosystems) and sequenced (paired end 150nt) on an Illumina NovaSeq 6000 system (Illumina).

Bulk RNA-seq analysis

The quality of raw sequence data was assessed using FastQC (v 0.11.9). Raw sequence was trimmed for adapter content using Trimmomatic (v 0.39) and aligned to the GRCm38.p6 genome using STAR (v 2.7.7a). Alignment quality was assess using Picard's CollectAlignmentMetrics, CollectRnaSeqMetrics, MarkDuplicates and CollectInsertSizeMetrics tools (v 2.25.1 for the spleen dataset and v 2.27.3 for the lung dataset). Quantification of gene expression was performed using Salmon (v 1.6.0 for the spleen dataset and v 1.9.0 for the lung dataset) in mapping-based mode versus the Ensembl release 102 transcriptome. Differential gene expression analysis was carried out using DESeq2 (v 1.34.0) in R (v 4.1.2). For the spleen dataset, batch effects between the two sequencing pools were accounted for by including the sequencing pool as a term in the linear model. The effectiveness of this strategy was confirmed using the `removeBatchEffect` function from the limma package (v 3.50.0) to generate a batch corrected counts matrix, followed by principal component analysis to assess remaining batch effects.

In the spleen dataset, 2 KO samples were excluded based on high *Tnfrsf4* expression, indicating mis-genotyping, and 3 poor quality samples were excluded based on low read counts. In the lung dataset, 2 ILC2 samples were excluded based on high *Foxp3* expression, indicating contamination of the sorted cells with Tregs.

Heatmaps were drawn using pheatmap (v 1.0.12), and gene set enrichment analyses were performed using clusterProfiler (v 4.4.4) and MSigDB gene set collection C7 (Immunological signatures, including the gene set GSE7852_TREG_VS_TCONV_FAT_UP(*14*)) in R. We used CellChat(*15*) to predict putative cell-cell communication pathways. As CellChat was developed for use in single-cell applications, we instead defined over-expressed genes as genes for which at least one sample has a normalised expression count exceeding 1000. Computation of communication probability was also performed using the 'truncatedMean' method, with trim=0.1.

TCR sequences analysis were extracted from RNA-seq data using MiXCR (v 4.0.0). Diversity metrics along with abundance analyses were carried out with the Immunarch package (v 0.8.0) in R.

scRNA-seq analysis
Publicly available scRNA-seq data of tumour-infiltrating Tregs from non-small cell lung cancer patients were obtained (*31*) (GSE235500). CellRanger output (barcodes.tsv.gz, features.tsv.gz, matrix.mtx.gz) of tumour samples was read in Seurat (v4.3.0), subsetting for cells with lower than 10% mitochondrial transcripts and more than 250 expressed genes. Data was log-normalized, variable features identified, scaled, and PCA performed using default parameters. Initial integration was performed using the 'rpca' method, which identified a $FOXP3^+$ cluster corresponding to regulatory T cells. This cluster was then subsetted and re-integrated using the Seurat CCA method, and a cluster of $FOXP3^-$ cells removed to

yield a final Seurat object corresponding to tumour-infiltrating Tregs. Expression of Treg-associated transcripts was performed using the FeaturePlot and VlnPlot commands implemented in Seurat.

Statistics

Analysis for two groups were calculated using an unpaired two-tailed Student's *t*-test; comparisons of more than two groups were calculated using a one-way analysis of variance (ANOVA) with Tukey post-analysis. All data were analysed using GraphPad Prism 9 (GraphPad Software) except for the histology scores, which were analysed using a permutation test in R (*perm.test* function of the R package *exactRankTests*). Results with $p \leq 0.05$ being considered significant (*), $p \leq 0.01 = **$, $p \leq 0.001 = ***$, $p \leq 0.0001 = ****$.

DATA AND SOFTWARE AVAILABILITY

Sequencing data have been deposited under the accession number GSE230599.
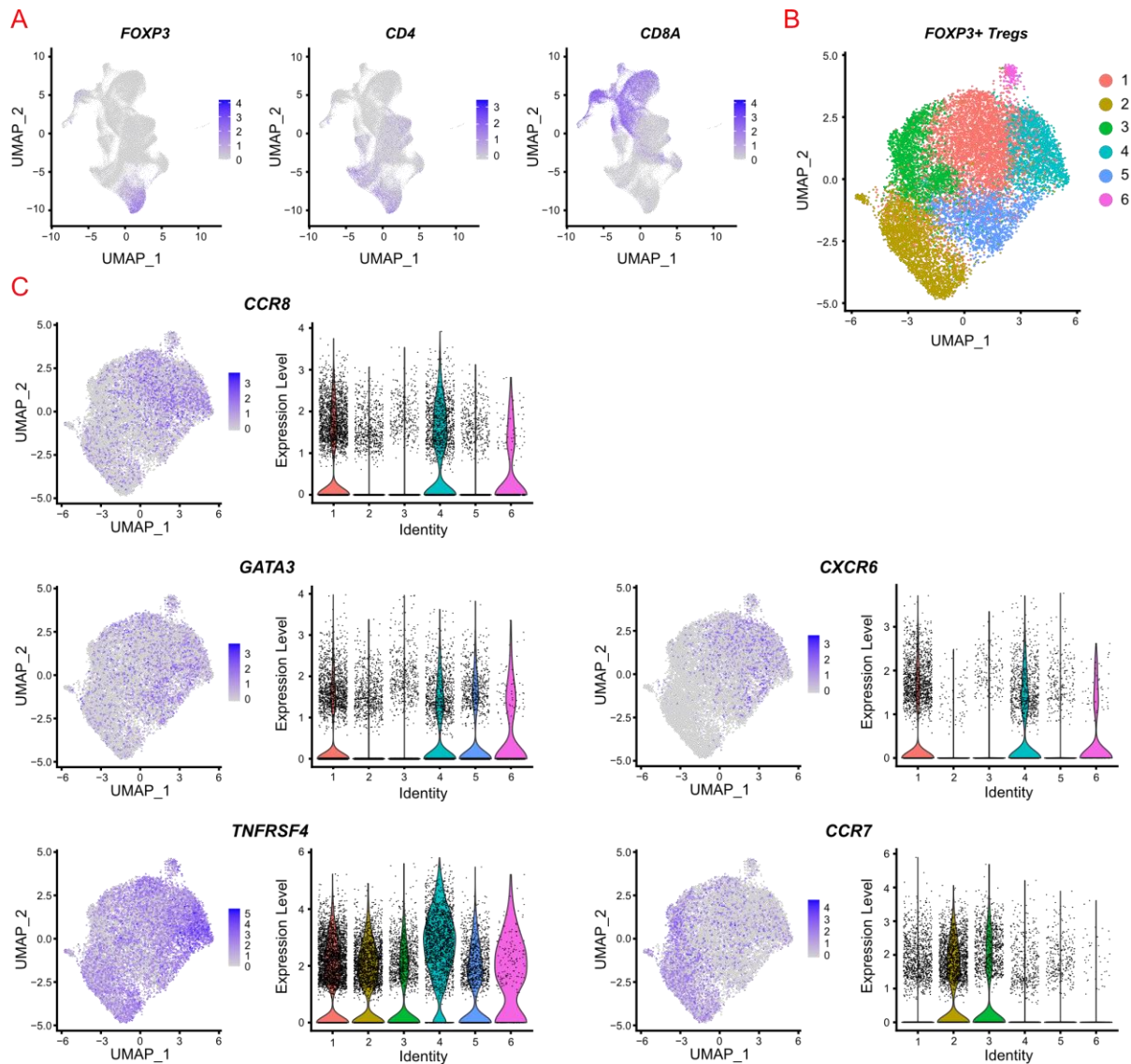
Supplemental Figures
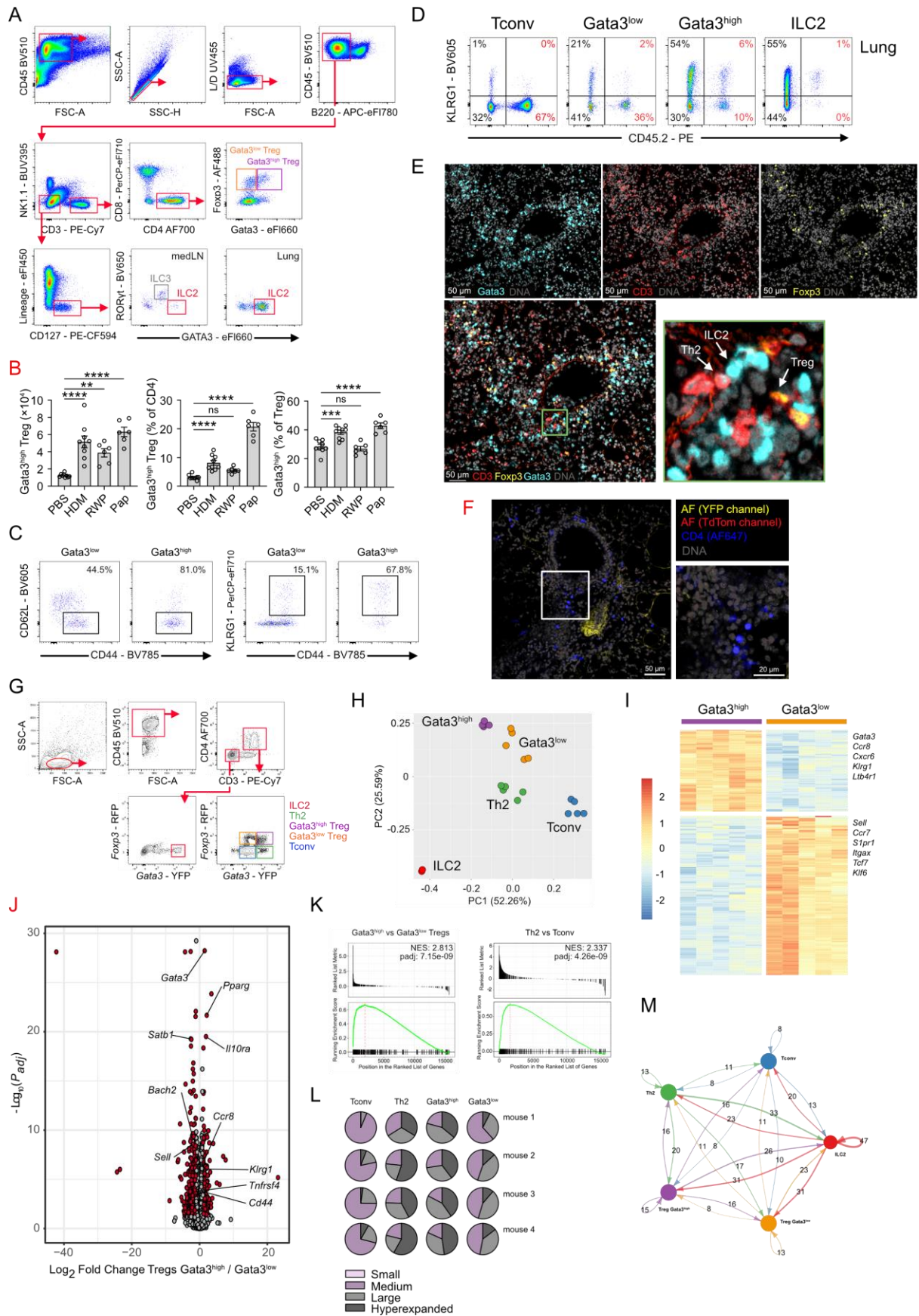
Supplemental Figure 1:

Gating strategy used to identify Gata3[high and low] Tregs and ILC2 (lung), and ILC3 (medLN) in IL-33-treated mice (**A**). C57Bl/6 mice were injected intranasally on day 0 and 1 with house dust mite (HDM), ragweed pollen extract (RWP), or papain (Pap), followed by analysis of lungs by flow cytometry for the indicated populations on day 5 (**B**). Dot plots showing the expression of CD44 and KLRG1 on Gata3[high and low] Tregs in the lungs of IL-33-treated mice (**C**). Dot plots showing the proportion of tissue-resident Tconv, Gata3[high and low] Tregs and ILC2 in the lungs of IL-33-treated mice after intravenous labelling with CD45.2 antibody (**D**). C57Bl/6 mice were injected with IL-33 (200 ng, i/n) on days 0 and 1, and sacrificed on day 5 followed by multiplex immunofluorescence imaging of lung sections; representative images of single channels (top) and merged (bottom, left) are shown, allowing the identification of nucleated CD3^{-}Gata3^{+} ILC2, CD3^{+}Gata3^{+} Th2 and CD3^{+}Foxp3^{+} Treg (bottom, right) (**E**). C57Bl/6 mice were injected with IL-33, followed by imaging of anti-CD4-treated precision cut lung slices using 2-photon microscopy; image shows the background fluorescence control for *Fig. 1D* (**F**).

G-M. *Gata3[YFP]Foxp3[RFP]* mice were injected with IL-33 (200 ng, i/n) on days 0 and 1, and sacrificed on day 5; lung ILC2 (CD45^{+}CD3^{-}CD4^{-}Foxp3[RFP-]Gata3^{high}), Foxp3[RFP+] Gata3^{high} and Gata3^{low} Tregs, and Foxp3[RFP-] Gata3^{high} Th2 and Gata3^{low} Tconv were flow-sorted for subsequent bulk-RNAseq analysis (**G**). Principal component analysis on the samples was performed (**H**). Differentially expressed genes were identified between Gata3^{high} and Gata3^{low} Treg populations; shown is a heatmap (**I**) or volcano plot (**J**) of identified genes with FDR < 0.0001; scale represents z-score. Gene-set enrichment analysis (using tissue-resident Treg geneset (*14*)) was performed on [Gata3^{high} vs Gata3^{low} Treg DEG] (left) and [Th2 vs Tconv DEG] (right) (**K**). TCR diversity analysis was performed on the transcriptomic data; pie charts show proportions of the indicated clonal subgroups in the indicated T cell populations for 4 out of 5 animals (mouse 5 is shown in *Fig. 1H*) (**L**). CellChat analysis was performed on the indicated populations to predict homotypic and heterotypic interactions; directionality indicated by arrow; the number represents the number of identified interactions (**M**).

Dot plots show representative gating strategy; numbers indicate percent of gated cells. Microscopy images are representative of 2 (**E, F**) independent experiments. Bar graphs indicate mean (±SEM) and show pooled data from 3 independent experiments (n=9,9,6,6; **B**) mice per group. ns = not significant, ** = p ≤ 0.01, *** = p ≤ 0.001, **** = p ≤ 0.0001.

Supplemental Figure 2

A-C. scRNA-seq data were obtained from patient-derived non-small cell lung cancer (NSCLC) samples (GSE235500) and re-integrated in Seurat using the reciprocal PCA method. This identified a cluster of $FOXP3^{+}CD4^{+}CD8^{-}$ tumour-infiltrating Tregs (**A**), that were subsequently integrated using the CCA integration method implemented in Seurat, and re-clustered into 6 cellular clusters (**B**, total 13547 cells). Single-cell expression levels of *CCR8, GATA3, CXCR6, TNFRSF4,* and *CCR7* across the 6 clusters (**C**).
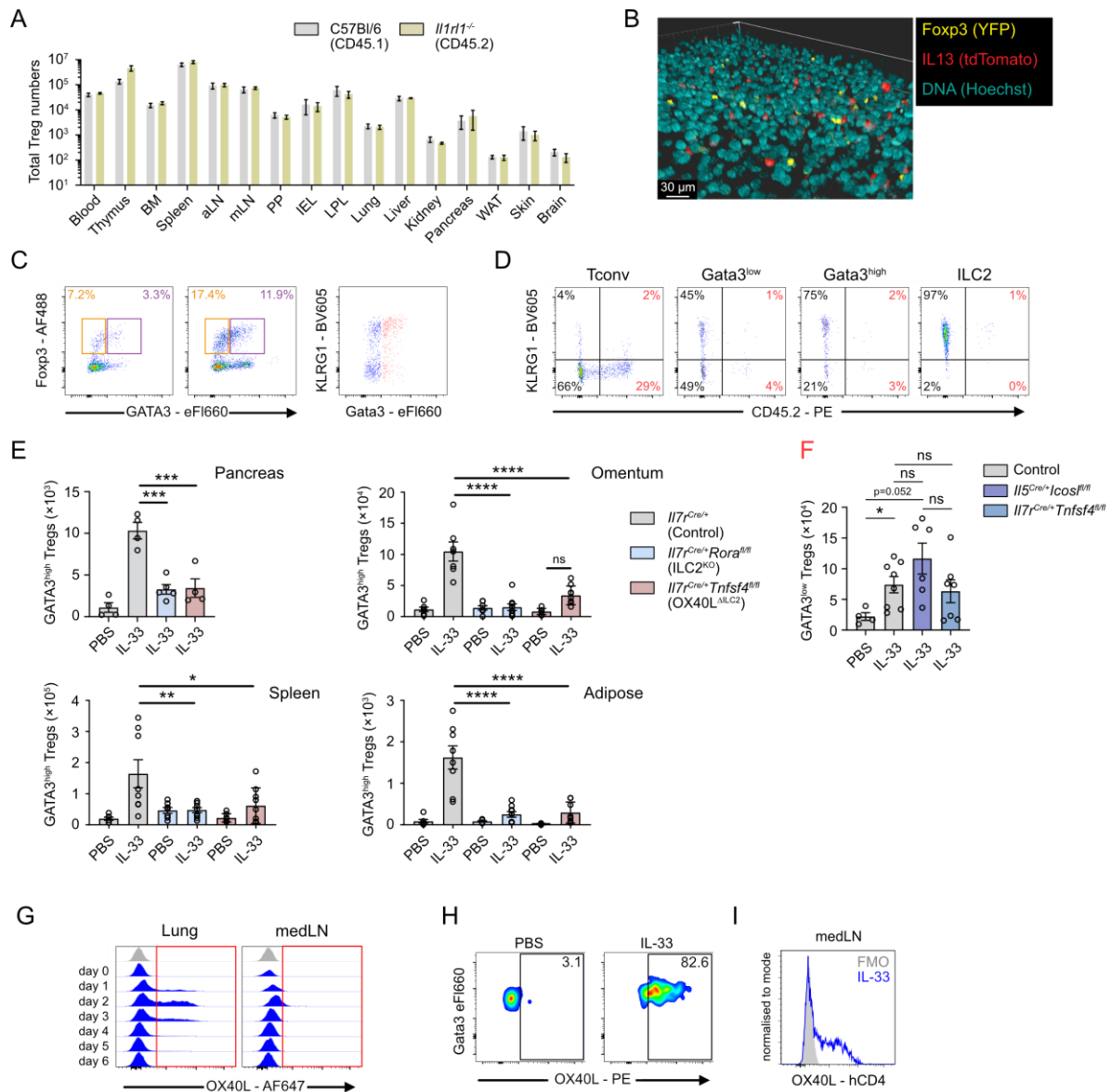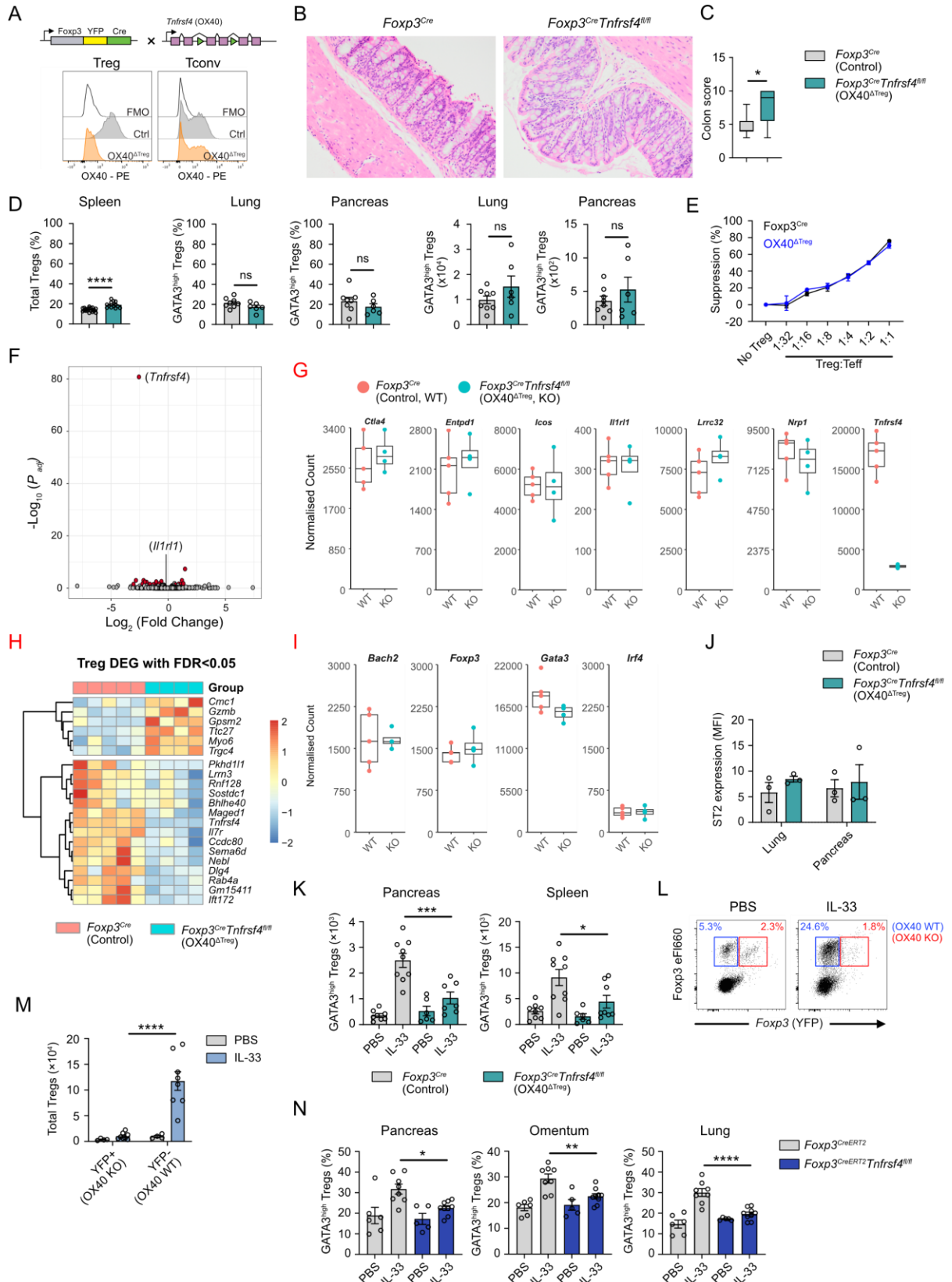
Supplemental Figure 3:

Donor derived wild-type (C57Bl/6) and *Il1rl1*^{-/-} Tregs were quantified in the indicated tissues of untreated (50:50, WT/KO) bone marrow chimeric mice (**A**). ILC2 (*Il13*[tdTom+]) and Tregs (*Foxp3*[YFP+]) were visualised in pancreas explants of IL-33-treated *Il13*[tdTom/+]*Foxp3*[YFP/y] mice (**B**).

C-D. PBS and IL-33-treated wild-type pancreata were analysed for KLRG1 expression on Gata3[high and low] Tregs (**C**). Dot plots showing the proportion of tissue-resident Tconv, Gata3[high and low] Tregs and ILC2 in the pancreas of IL-33-treated mice after intravenous labelling with CD45.2 antibody (**D**).

E-F. Mice of the indicated genotypes were intraperitoneally dosed with PBS or IL-33 on day 0 and 1, followed by quantification of Gata3^{high} Treg (**E**) or Gata3^{low} Treg (**F**) numbers in the indicated organs on day 5.

G-I. Histograms showing OX40L expression on ILC2 from wild-type mice dosed with IL-33 i/n on days 0 and 1, followed by the analysis of lungs and medLN at the indicated time points (**G**). Representative dot plot showing OX40L expression on pancreatic ILC2 from wild-type mice dosed with IL-33 i/p on days 0 and 1 and analysed on day 2 (**H**). Representative dot plot showing hCD4 expression on medLN ILC2 from *Tnfsf4$^{hCD4/+}$* mice dosed with PBS or IL-33 i/n on days 0 and 1 and analysed on day 3 (**I**).

Dot plots show representative gating strategy; numbers indicate percent of gated cells. Two photon microscopy indicates representative region from 2 independent experiments. Bar graphs indicate mean (±SEM) and show data of one experiment (n=4 for all; **A**), or representative data of 3 independent experiments (n=4,4,5,4; **E**, panc.) or pooled data from 2 independent experiments, (n=6,7,7,9,7,9, Omentum, **E**), (n=6,8,7,9,7,9, Spleen, **E**), (n=6,7,7,9,7,8, Adipose, **E**), (n=4,8,6,7, Lung, **F**) mice per group. * = p ≤ 0.05, ** = p ≤ 0.01, *** = p ≤ 0.001, **** = p ≤ 0.0001.
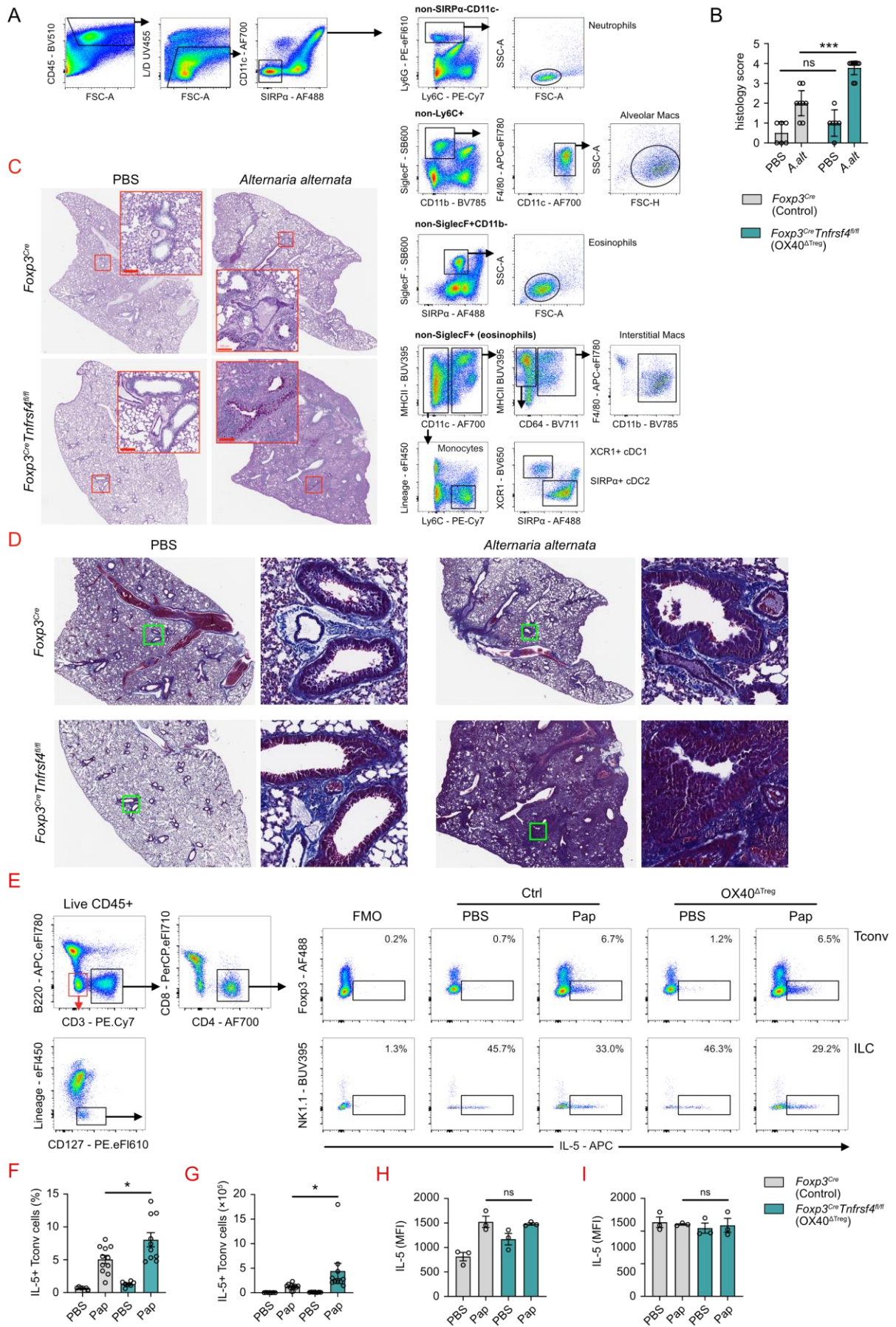
Supplemental Figure 4:

A-J. Schematic representation of the alleles crossed to generate OX40$^{\Delta Treg}$ mice (top), and histograms showing OX40 staining on spleen Treg and Tconv cells from OX40$^{\Delta Treg}$ and control mice upon *in vitro* restimulation with anti-CD3/CD28 coated beads (bottom) (**A**).

Representative H&E sections of colons from OX40$^{\Delta Treg}$ and control mice (**B**). Histology scoring of colon sections as shown in (**B**) (**C**). Quantification of total Tregs (% of CD4$^+$) and Gata3^{high} Tregs (numbers and % of Tregs) in the spleen, lung and pancreas of OX40$^{\Delta Treg}$ and control mice (**D**). *In vitro* suppression assay with splenic Tregs isolated from OX40$^{\Delta Treg}$ or control mice and co-cultured with Tconv for 5 days (**E**). Volcano plot of the differentially expressed genes between spleen Tregs from OX40$^{\Delta Treg}$ and control mice. Red dots indicate genes with a FDR <0.05 and log2FC |>1.5|, and include *Tnfrsf4*, but not *Il1rl1* (**F**). Expression of selected genes encoding surface proteins in spleen Tregs from OX40$^{\Delta Treg}$ and control mice (**G**). Heatmap of the differentially expressed genes with a FDR <0.05 and log2FC |>1.5| between spleen Tregs from OX40$^{\Delta Treg}$ and control mice (**H**). Expression of selected genes encoding transcription factors in spleen Tregs from OX40$^{\Delta Treg}$ and control mice (**I**). ST2 expression on Gata3^{high} Tregs from the lungs and pancreas of OX40$^{\Delta Treg}$ or control mice (**J**).

K-M. OX40$^{\Delta Treg}$ or control mice were intraperitoneally dosed with PBS or IL-33 on day 0 and 1, followed by quantification of Gata3^{high} Treg numbers in the spleen and pancreas on day 5 (**K**). *Foxp3$^{Cre/+}$Tnfrsf4$^{fl/fl}$* hemizygous female mice were intraperitoneally dosed with PBS or IL-33 on day 0 and 1 and sacrificed on day 5. Dot plot showing the gating of YFP$^+$ and YFP$^-$ lung Tregs (**L**), and lung total Treg numbers (**M**).

Foxp3^{CreERT2}Tnfrsf4$^{fl/fl}$ or control mice were given tamoxifen diet for a week, before being intraperitoneally dosed with PBS or IL-33 on day 0 and 1, followed by quantification of Gata3^{high} Treg as a % of Treg cells in pancreas, omentum and lung on day 5 (**N**).

Bar graphs indicate mean (±SEM) and show representative data of one experiment (n=3,3,3,3; **J**), or pooled data from 2 independent experiments (n=9,9; **C**), (n=19,13; spleen; n=8,6; lung and pancreas; **D**), (n=8,9,6,7; for all in **K**), (n=4,9,4,8; **M**), (n= 6,8,5,9; for all in **N**) mice per group. * = p ≤ 0.05, ** = p ≤ 0.01, *** = p ≤ 0.001, **** = p ≤ 0.0001.
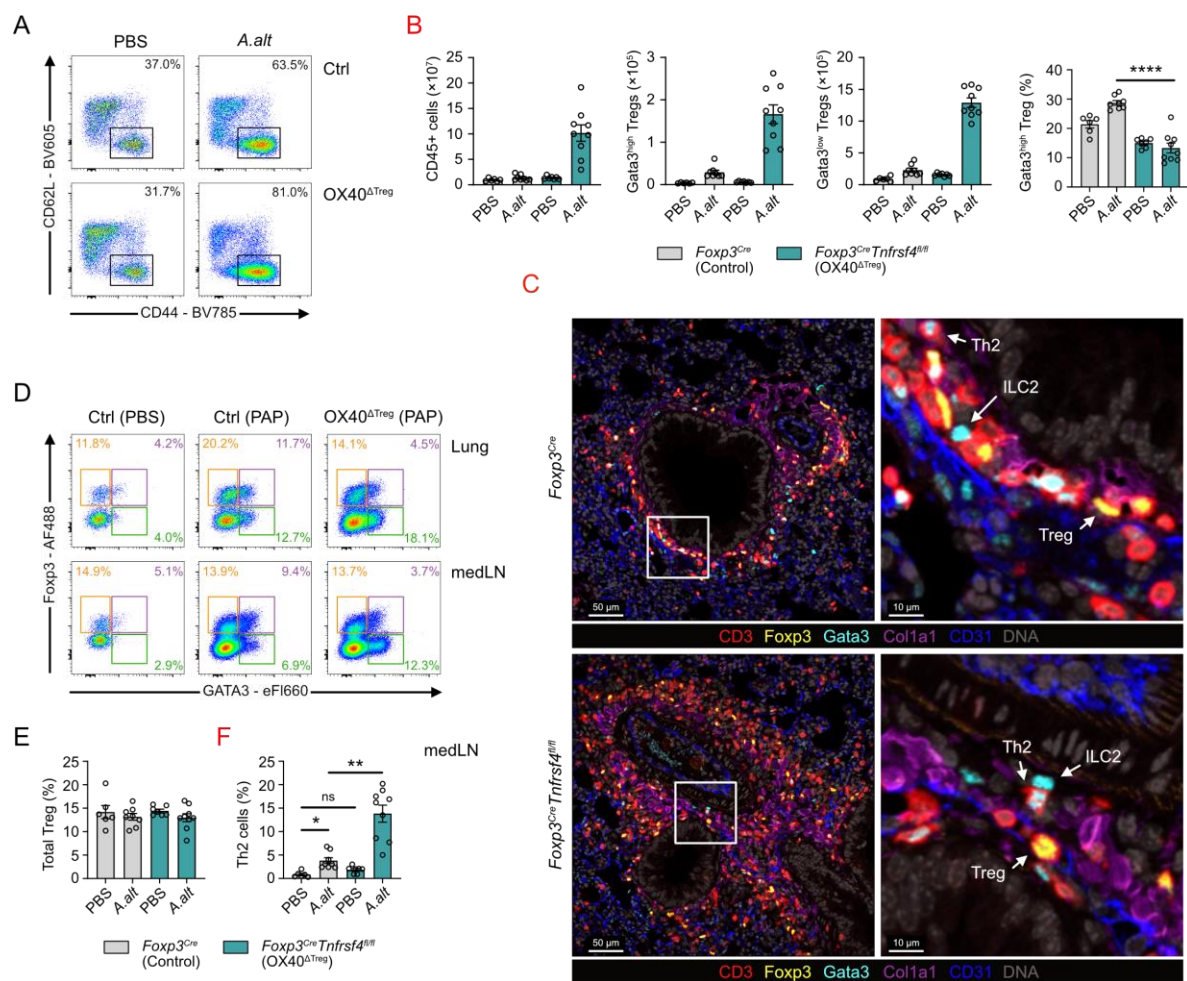
Supplemental Figure 5:

A. Gating strategy used to identify the indicated populations in the lung (**A**).

B-D. OX40$^{\Delta Treg}$ or control mice were treated intranasally with *Alternaria alternata* or PBS on days 0, 1 and 14, followed by sacrifice on day 20. Histology scoring of H&E lung sections (**B**), representative images of PAS staining on lung sections (**C**), and representative images of Masson's Trichrome staining on lung sections (**D**).

E-I. OX40$^{\Delta Treg}$ or control mice were treated intranasally with papain (Pap) or PBS on days 0, 1 and 14, followed by sacrifice on day 20. Lung cells were stimulated *ex vivo* with PMA + ionomycin and protein export inhibitor cocktail for 3 hours, followed by intracellular staining for IL-5. Representative dot plots are shown in (**E**). The percentage of IL-5$^+$ T cells amongst CD4$^+$ T cells (**F**), total numbers of lung IL-5$^+$ Tconv cells (**G**), and the mean fluorescence intensity of IL-5$^+$ Tconv (**H**) or IL-5$^+$ ILCs (**I**) were measured.

Dot plots show representative gating strategy. Bar graphs indicate mean (±SEM) and show pooled (n=6,8,7,9; **B**), (n=7,11,7,10; **F, G**) or representative (n=3,3,3,3; **H** and **I**) data from 3 independent experiments. ns = not significant, *** = p ≤ 0.001.
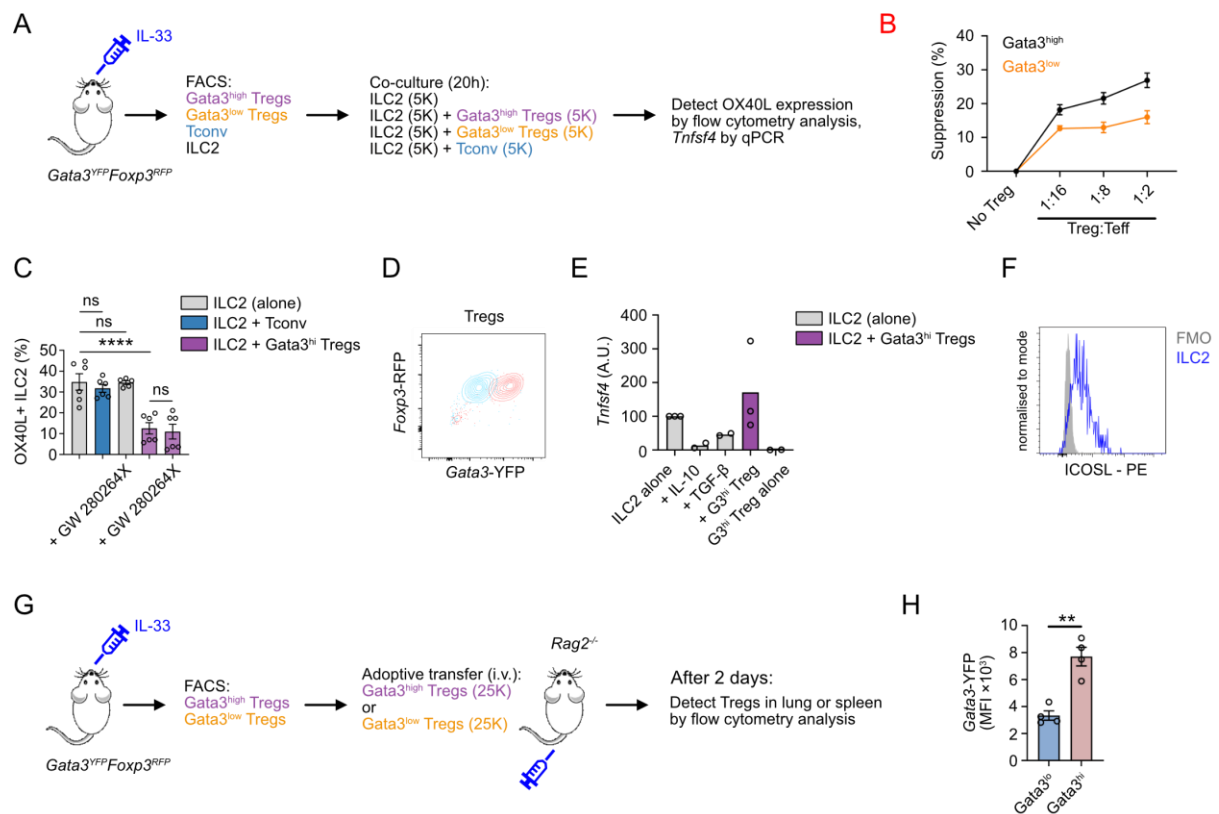
Supplemental Figure 6:

A-F. OX40$^{\Delta Treg}$ or control mice were treated intranasally with *Alternaria alternata* or PBS on days 0, 1 and 14, followed by sacrifice on day 20. Dot plots showing the proportion of CD44$^+$CD62L$^-$ cells among total CD4$^+$ T cells, which are further gated on in *Fig. 4A* (**A**). Flow cytometric quantification of CD45$^+$ and Gata3^{high} and Gata3^{low} Treg cell numbers, and percent of Gata3^{low} Tregs (% of total CD44$^+$CD62L$^-$CD4$^+$) (**B**). Formalin-fixed paraffin-embedded cut lung sections were stained for multiplex immunofluorescence imaging using antibodies directed against CD3, Foxp3, Gata3, Collagen-I, and CD31. DNA was stained using DAPI. (**C**). Dot plots showing the gating strategy used to quantify Gata3^{high} and Gata3^{low} Tregs (purple and orange quadrants, respectively) and Th2 cells (green quadrant) (**D**). Flow cytometric quantification of total Treg percentage (% of total CD4$^+$) (**E**) and Th2 (% of total CD4$^+$) (**F**) in the medLN.

Microscopy images (C) are representative of lung sections obtained from 3 mice per group from 1 experimental setup. Dot plots show representative gating strategy; numbers indicate percent

of gated cells. Bar graphs indicate mean (±SEM) and show pooled data from 2 independent experiments (n=6,8,7,9; **B**, **E**, **F**) mice per group. ns = not significant, *** = $p \leq 0.001$.
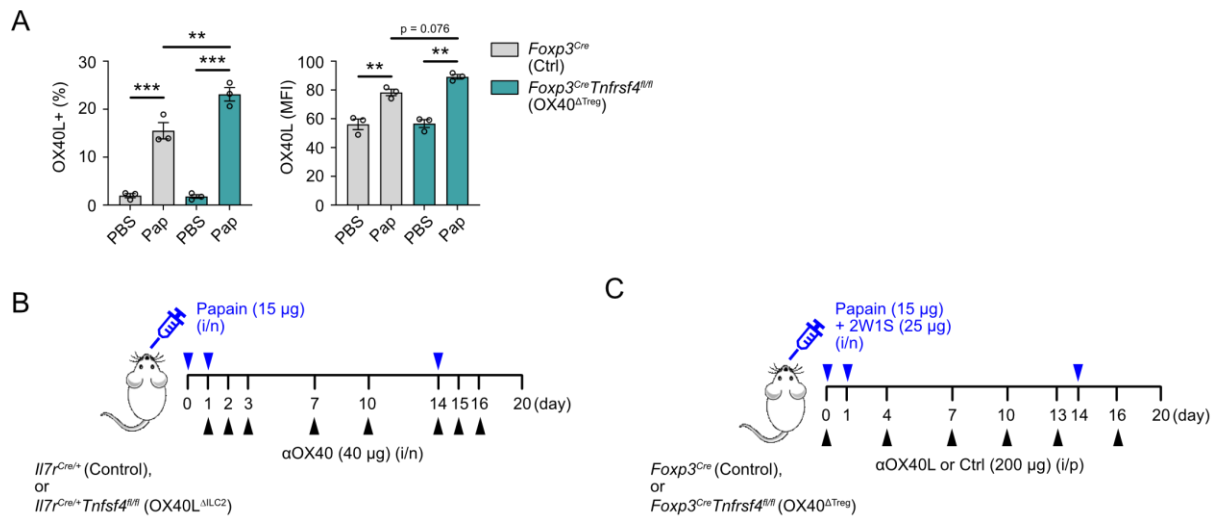
Supplemental Figure 7:

A-F. *Gata3^{YFP}Foxp3^{RFP}* mice were injected with IL-33 (i/n) on days 0 and 1, and sacrificed on day 5; lung ILC2, Tconv, Gata3^{high} and Gata3^{low} Tregs were flow-sorted. *In vitro* suppression assay with lung Gata3^{high} and Gata3^{low} Tregs co-cultured with Tconv for 4 days (**B**). Lung cell populations were cultured overnight as mono- or co-cultures in the presence of IL-2, IL-7 and IL-33 and where indicated (*here or in Fig. 5*) with additional anti-IL10, anti-IL10R, anti-TGF-β, anti-ICOSL, anti-OX40, anti-PD-1, anti-ICAM1, Pitstop-2, ADAM10/17 inhibitor (GW 280264X), A2A receptor inhibitor, POM1 inhibitor, IL-10 or TGF-β1. Cells were subsequently harvested and stained for OX40L expression on ILC2 by flow cytometry (**C**). Representative signal of Foxp3-RFP and Gata3-YFP (gated on Live CD45$^+$CD3$^+$CD4$^+$ T cells) on Gata3^{high} (red) or Gata3^{low} (blue) sorted Tregs after 20 hours of co-culture (**D**). Cells co-cultured overnight as in (A) were subjected to RNA extraction followed by quantification of *Tnfsf4* transcript by RT-qPCR (**E**). ILC2 in co-cultures were analysed for ICOSL surface expression (**F**).

G-H. Gata3^{high} or Gata3^{low} Tregs were flow-sorted as in (A), followed by adoptive transfer of 2.5×10^4 cells into *Rag2$^{-/-}$* recipient mice (treated with IL-33 i/n one day before transfer); recipient mice were sacrificed 2 days after Treg transfer, followed by quantification of Live

CD45$^+$CD3$^+$CD4$^+$Foxp3^{RFP+} Tregs in the lungs or spleens by flow cytometry analysis (**G**). The mean fluorescence intensity (MFI) of Gata3-YFP was measured on Treg subsets recovered in the spleen (**H**).

Dot plot and histogram shows representative data of at least 2 independent experiments. Bar graphs indicate mean (±SEM) and show representative data of 2 independent experiments (n=4 per condition; **B**), or combined data of 2-3 independent experiments (n=6,6,6,6,6; **C**, n=3,2,2,3,2; **D**), or 3 independent experiments with (n=4,4; **H**) mice. ns = not significant, ** = p ≤ 0.01, *** = p ≤ 0.001.

Supplemental Figure 8:

A. Mice of the indicated genotypes were injected intranasally with PBS or papain protease allergen on days 0 and 1, followed by analysis of percent positive (left) and mean fluorescence intensity (right) of OX40L on lung ILC2 using flow-cytometry analysis on day 2.

B. Experimental layout for *Fig. 6A-B*; mice of the indicated genotypes were dosed intranasally with papain (15 µg) on days 0, 1, and 14, and intranasally with OX40 mAb agonist (40 µg) on the indicated days.

C. Experimental layout for *Fig. 6C-F* (without 2W1S) or *Fig. 6G* (with 2W1S); mice of the indicated genotypes were dosed intranasally with *Alternaria alternata* extract (10 µg) (+/- 2W1S, 25 µg), and intraperitoneally with OX40L mAb antagonist or control IgG (200 µg) on the indicated days.

Bar graphs indicate mean (±SEM) and show 1 experiment with (n=3,3,3,3; **A**) mice, ** = $p \leq$ 0.01, *** = $p \leq 0.001$.

Supplemental Table 1

Supplemental Table 2